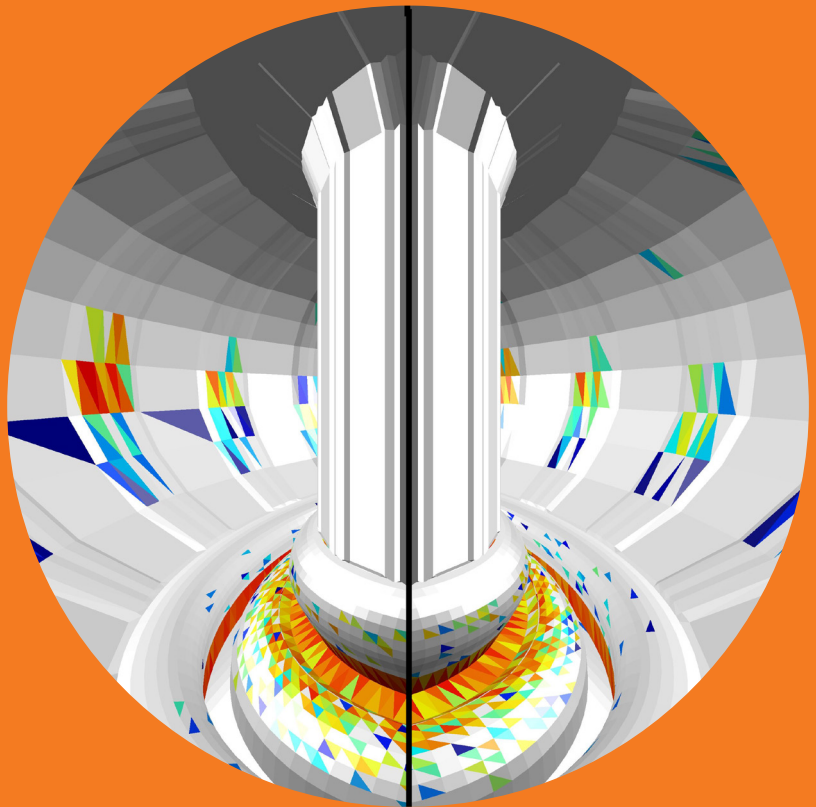


Monte Carlo simulation of fast ion losses in ITER in the presence of static 3D magnetic perturbations

Tuomas Koskela



Monte Carlo simulation of fast ion losses in ITER in the presence of static 3D magnetic perturbations

Tuomas Koskela

A doctoral dissertation completed for the degree of Doctor of Science (Technology) to be defended, with the permission of the Aalto University School of Science, at a public examination held at the lecture hall k216 of the school on 9 January 2015 at 12.

Aalto University
School of Science
Department of Applied Physics
Fusion and Plasma Physics

Supervising professor

Prof. Mathias Groth, Aalto University, Finland

Thesis advisor

Prof. Taina Kurki-Suonio, Aalto University, Finland

Preliminary examiners

Dr. Sergei Sharapov, Culham Centre for Fusion Energy, UK

Dr. Lars-Göran Eriksson, European Commission, DG Research, Unit
G6 - Fusion Energy, Belgium

Opponent

Dr. Simon Pinches, ITER Organisation, France

Aalto University publication series

DOCTORAL DISSERTATIONS 202/2014

© Tuomas Koskela

ISBN 978-952-60-6003-3 (printed)

ISBN 978-952-60-6004-0 (pdf)

ISSN-L 1799-4934

ISSN 1799-4934 (printed)

ISSN 1799-4942 (pdf)

<http://urn.fi/URN:ISBN:978-952-60-6004-0>

Unigrafia Oy
Helsinki 2014

Finland



Author

Tuomas Koskela

Name of the doctoral dissertation

Monte Carlo simulation of fast ion losses in ITER in the presence of static 3D magnetic perturbations

Publisher School of Science

Unit Department of Applied Physics

Series Aalto University publication series DOCTORAL DISSERTATIONS 202/2014

Field of research Plasma Physics

Manuscript submitted 4 September 2014

Date of the defence 9 January 2015

Permission to publish granted (date) 24 October 2014

Language English

☐ **Monograph**

☒ **Article dissertation (summary + original articles)**

Abstract

The confinement of fast ions is of paramount importance for future nuclear fusion reactors, such as ITER. Confined fast ions are needed to heat the plasma into fusion-relevant temperatures, while fast ion losses may compromise the integrity of the vacuum vessel. Fast ions are well confined in an axisymmetric tokamak with a high plasma current, but even small deviations from axisymmetry may lead to localized fast ion losses that may compromise the operation of the machine.

This thesis describes Monte Carlo simulations of fast ion confinement and losses in ITER as well as existing tokamaks. Since fast ions are relatively collisionless, the theory of collisionless orbits of charged particles in tokamak geometry is first discussed. The collisionless orbits are perturbed by the infrequent collisions with the background plasma and by deviations from magnetic axisymmetry, which. To study these orbits in realistic tokamaks, the theory is put into use in the ASCOT code, whose main features are described in the thesis. Finally, as simulations need to be connected with experiments, the most commonly used fast ion diagnostics are described and their connections to simulations discussed.

The results obtained in this thesis are encouraging for the operation of ITER. The ASCOT code has been benchmarked with several fast ion diagnostics as well as other codes, and satisfactory agreement has been found. The predictive modelling of ITER suggests that the toroidal field ripple will induce significant fast ion losses, but it can be effectively mitigated by ferritic inserts. The perturbation due to the magnetization of the ferritic steel in test blanket modules is not seen as a threat to fast ion confinement. The impact of ELM control coils on fast ion losses needs more study, but it seems likely that the plasma will screen the error field inside the pedestal, preventing the high fast ion losses seen in vacuum models.

Keywords fusion, plasma, tokamak, ITER, modeling

ISBN (printed) 978-952-60-6003-3

ISBN (pdf) 978-952-60-6004-0

ISSN-L 1799-4934

ISSN (printed) 1799-4934

ISSN (pdf) 1799-4942

Location of publisher Helsinki

Location of printing Helsinki

Year 2014

Pages 176

urn <http://urn.fi/URN:ISBN:978-952-60-6004-0>

Tekijä

Tuomas Koskela

Väitöskirjan nimi

Nopeiden hiukkasten häviöiden 3D Monte Carlo -mallinnus ITER-tokamakissa

Julkaisija Perustieteiden korkeakoulu

Yksikkö Teknillisen fysiikan laitos

Sarja Aalto University publication series DOCTORAL DISSERTATIONS 202/2014

Tutkimusala Plasmafysiikka

Käsikirjoituksen pvm 04.09.2014

Väitöspäivä 09.01.2015

Julkaisuluvan myöntämispäivä 24.10.2014

Kieli Englanti

☐ **Monografia**

☒ **Yhdistelmäväitöskirja (yhteenvedo-osa + erillisartikkelit)**

Tiivistelmä

Nopeiden ionien koossapito on ehdottoman tärkeää tulevissa fuusioreaktoreissa, kuten ITER:ssä. Koossapidetyt nopeat hiukkaset luovuttavat liike-energiaansa plasmaan, kuumentaen sen fuusioon vaadittavaan lämpötilaan, mutta toisaalta koossapidosta paenneet nopeat ionit ovat uhka reaktorikammion eheydelle. Aikaisempi tutkimus on osoittanut että nopeat ionit pysyvät hyvin koossapidettyinä aksiaalisesti symmetrisissä tokamakeissa joissa on korkea plasmavirta, mutta häviävän pienet poikkeamat symmetriasta voivat aiheuttaa paikallisia häviöitä jotka voivat vaarantaa koko reaktorin toiminnan.

Tässä väitöskirjatyössä on tutkittu nopeiden hiukkasten koossapitoa ja häviöitä ITER:ssä sekä olemassaolevissa tokamak-reaktoreissa numeerisen Monte Carlo -mallinnuksen keinoin, joka pohjautuu hiukkasten ratojen seurantaan. Koska nopeat hiukkaset ovat lähes törmäyksettömiä, käydään ensin läpi yhtälöt, jotka kuvaavat törmäyksettömien hiukkasten ratoja aksisymmetrisissä tokamakeissa. Todellisuudessa hiukkaset poikkeavat törmäyksettömiltä radoilta törmäysten sekä magneettisten epäsymmetrioiden takia. Näitä ratoja seurataan ASCOT-koodilla, jonka tärkeimmät ominaisuudet esitellään työn menetelmäosiossa. Simulaatiotulosten validoimiseksi niitä on verrattava olemassaolevissa koelaitteissa saatuihin mittaustuloksiin. Tärkeimmät nopeiden hiukkasten mittalaitteet ja tavat niiden signaalien mallintamiseen käsitellään lopuksi.

Työn tuloksena saadut ennusteet ITER:lle ovat rohkaisevia. ASCOTin antamat tulokset vastaavat hyvin useita nopeiden hiukkasten mittauksia ja riippumattomia mallinnustuloksia olemassaolevilla koelaitteilla. ITERin ennustavat mallinnustulokset osoittavat, että magneettikentän väreily kelaväleissä aiheuttaa suuria nopeiden hiukkasten häviöitä, mutta sitä voidaan tehokkaasti vaimentaa ferriittisillä inserteillä. Sen sijaan tritiumin hyötöön käytettävissä moduuleissa olevan ferriittisen teräksen magnetoitumasta aiheutuvat häiriöt eivät vaaranna nopeiden hiukkasten koossapitoa merkittävästi. Reunaplasman epästabiiliuksien ehkäisyyn käytettävien häirökelojen mallinnusta on vielä jatkettava, mutta näyttää todennäköiseltä että niiden aiheuttamat häiriöt vaimenevat reunaplasman sisäpuolella eivätkä aiheuta suuria nopeiden hiukkasten häviöitä.

Avainsanat fuusio, plasma, tokamak, ITER, mallinnus

ISBN (painettu) 978-952-60-6003-3

ISBN (pdf) 978-952-60-6004-0

ISSN-L 1799-4934

ISSN (painettu) 1799-4934

ISSN (pdf) 1799-4942

Julkaisupaikka Helsinki

Painopaikka Helsinki

Vuosi 2014

Sivumäärä 176

urn <http://urn.fi/URN:ISBN:978-952-60-6004-0>

Preface

The research work in this thesis was carried out at the department of applied physics in the Aalto University School of Science, Espoo, Finland from 2009 to 2012 and at Culham Centre for Fusion Energy, Abingdon, United Kingdom from 2012 to 2014. During my journey across Europe in pursuit of fusion energy, I've made many good friends and acquaintances.

I would like to thank my supervisor Taina Kurki-Suonio for her guidance and encouragement during my studies. I would also like to thank my supervising professors, Rainer Salomaa for giving me the chance to work in fusion research and Mathias Groth for keeping me focused on my thesis after going to CCFE. The fusion group at Aalto University was truly a great environment to work and I would like to thank Otto, Simppa, Antti, Eero and all the others for the relaxed and friendly atmosphere.

At CCFE, I would like to thank my line manager Dr. Michele Romanelli for allowing me to finish my studies at the leading fusion lab in Europe, the experience of the last two years has really been eye-opening. I am also deeply grateful to all my friends and colleagues at Culham who have made me feel welcome and made my new life in England enjoyable both in and out of the office.

Last, but not least, I would like to thank my wonderful girlfriend Heli, for embarking on this adventure with me, and for supporting and pushing me on in tough times. I also thank my family and friends for keeping in touch during my travels, and for your hospitality during my visits.

CCFE, Abingdon, Oxfordshire, United Kingdom, December 1, 2014,

Tuomas Koskela

Contents

Preface	1
Contents	3
List of Symbols	5
List of Publications	9
Author's Contribution	11
1. Introduction	13
1.1 Tokamaks	15
1.2 New physics explored in ITER	19
1.3 Scope of the thesis	21
2. Fast Ions in Tokamak Environment	23
2.1 Fast ion motion	25
2.1.1 Collisionless orbits in toroidal geometry	27
2.1.2 Interactions in a plasma	29
2.2 The breaking of axisymmetry in tokamaks	31
2.2.1 Toroidal field ripple	31
2.2.2 Magnetized components	34
2.2.3 External coils	37
3. Tools and Methods	41
3.1 ASCOT	41
3.1.1 Brief history of ASCOT	42
3.1.2 Background data	43
3.1.3 Fast ion sources	45
3.1.4 Monte Carlo orbit following	47
3.1.5 Numerical diagnostics	48

3.2	JINTRAC	51
3.2.1	ASCOT in JINTRAC	52
3.3	Tokamaks of interest	53
3.4	Measuring the fast ion distribution	54
4.	Results	59
4.1	Fast ion studies on existing tokamaks	59
4.1.1	Modelling the effect of the JET ITER-like wall on neutral beam deposition	60
4.1.2	Modelling of local CTS measurements of fast ion den- sity in TEXTOR	64
4.1.3	Fast ion losses in DIII-D TBM mock-up experiments .	66
4.2	Predictions of fast ion wall loads in ITER	68
4.2.1	Fast ion losses due to toroidal field ripple	69
4.2.2	Fast ion losses due to test blanket modules	73
4.2.3	Fast ion losses due to ELM control coils	74
5.	Summary and Future Prospects	77
	Errata	81
	Publications	83
	Bibliography	159

List of Symbols

δ	Toroidal field ripple strength
ϵ	Inverse aspect ratio
ϵ'	Ordering parameter
Γ	Particle flux
γ	Lorentz factor
$\hat{\mathbf{b}}$	Magnetic field unit vector
\mathcal{R}	Fusion reaction rate
μ	Magnetic moment
ν	Collisionality
Ω	Gyrofrequency
ω	Angular frequency of plasma rotation
Φ	Scalar potential
ϕ	Toroidal angle
ψ	Poloidal flux function
ψ_n	Normalized poloidal flux function
ρ	Square root of normalized poloidal flux
σ	Atomic cross-section
τ	Torque
θ	Geometric poloidal angle
θ_g	Gyrophase

A	Vector potential
B	Magnetic field
E	Electric field
J	Current density
r	Position vector of the particle
r_L	Larmor radius vector
r_{GC}	Position vector of the guiding center
u_E	$\mathbf{E} \times \mathbf{B}$ drift velocity of the guiding center
v	Velocity vector of the particle
v_D	Drift velocity of the guiding center
ξ	Pitch angle cosine (v_{\parallel}/v)
B	Magnetic field strength
B_p	Poloidal magnetic field strength
B_R	Radial magnetic field strength
B_t	Toroidal magnetic field strength
B_z	Vertical magnetic field strength
c	Speed of light
D	Diffusion coefficient
e	Unit charge
f	Distribution function
f'	Poloidal current function
I_p	Plasma current
M	Mass number
m	Mass
m*	Effective impurity mass
N	Toroidal mode number

n	Particle density
N_c	Number of toroidal field coils
p	Scalar pressure
p_{\parallel}	Parallel momentum
P_{ϕ}	Toroidal canonical momentum
Q	Fusion power gain
q	Safety factor
R	Major radius, distance along major radius
r_L	Length of the Larmor radius
t	Time
v_{\parallel}	Parallel velocity of the particle/guiding center
v_{\perp}	Perpendicular velocity of the particle
W	Kinetic energy
w	Particle weighing factor
Z	Charge number
z	Distance along the vertical axis

List of Publications

This thesis consists of an overview and of the following publications which are referred to in the text by their Roman numerals.

- I** T. Koskela, M. Romanelli, P. Belo, O. Asunta, S. Sipilä, M. O’Mullane, L. Giacomelli, S. Conroy, P. Mantica, M. Valisa, C. Angioni, T. Kurki-Suonio and JET-EFDA contributors. Effect of tungsten off-axis accumulation on Neutral Beam Deposition in JET rotating plasmas.. *Submitted to Plasma Physics and Controlled Fusion*, 2014.
- II** D. Moseev, F. Meo, S. B. Korsholm, T. Koskela, M. Albergante, O. Asunta, H. Bindslev, A. Bürger, V. Furtula, M. Yu Kantor, F. Leipold, P. K. Michelsen, S. K. Nielsen, M. Salewski, O. Schmitz, M. Stejner, E. Westerhof. Comparison of measured and simulated fast ion velocity distributions in the TEXTOR tokamak. *Plasma Physics and Controlled Fusion*, 53, 10, 105004, August 2011.
- III** T. Koskela, O. Asunta, G. J. Kramer, T. Kurki-Suonio, A. Salmi, M. Schaffer, T. Tala. ASCOT modeling of fast ion losses in DIII-D TBM experiments. In *37th European Physical Society Conference on Plasma Physics*, Dublin, Ireland, Europhysics Conference Abstracts, 34A, 1-4, June 2010.
- IV** T. Kurki-Suonio, O. Asunta, V. Hynönen, T. Hellsten, T. Johnson, T. Koskela, J. Lönnroth, V. Parail, M. Rocella, G. Saibene, A. Salmi, S. Sipilä. ASCOT Simulations of Fast Ion Power Loads to the Plasma-facing Components in ITER. *Nuclear Fusion*, 49, 9, 095001, August 2009.

V T. Koskela, O. Asunta, E. Hirvijoki, T. Kurki-Suonio, S. Äkäslompolo.
ITER ELM control coils: effect on fast ion losses and edge confinement
properties. *Plasma Physics and Controlled Fusion*, 54, 105008, August
2012.

Author's Contribution

Publication I: “Effect of tungsten off-axis accumulation on Neutral Beam Deposition in JET rotating plasmas.”

This publication deals with the effect of heavy impurities on the dynamics of NBI ions in rotating plasmas. Due to a redistribution by the centrifugal force, heavy impurities were found to accumulate in the path of the beam and shift the fast ion distribution by increasing their ionization and scattering. The author developed the theoretical model for tungsten redistribution with M. Romanelli and implemented it into the ASCOT code and into a postprocessing tool for the JETTO code. The author performed the simulations presented in the paper and the comparisons to the experimental data provided by the coauthors. The author wrote the full paper.

Publication II: “Comparison of measured and simulated fast ion velocity distributions in the TEXTOR tokamak”

This publication presents a benchmark between the CTS diagnostic at the TEXTOR tokamak and ASCOT. Good agreement was found when measuring the fast ion distribution close to the magnetic axis. The author prepared the ASCOT simulation model of TEXTOR in collaboration with O. Asunta, D. Moseev and O. Schmitz. The author performed the ASCOT simulations described in the paper, and contributed to the analysis. The author co-wrote sections 4, 6 and 7 of the paper.

Publication III: “ASCOT modeling of fast ion losses in DIII-D TBM experiments”

This publication is a part of a modelling effort to interpret experiments where a localized magnetic perturbation was introduced into the DIII-D tokamak to study the effect of TBMs in ITER. The ASCOT code predicted the formation of a hot spot on the wall, which was confirmed experimentally as well as by other codes. The author performed the ASCOT simulations described in the paper and corresponded with the co-authors to set up and analyze them. The author developed the visualization tools used in the paper and performed the analysis presented in all the figures in the paper. The author wrote the full paper and presented it in the 37th EPS conference.

Publication IV: “ASCOT Simulations of Fast Ion Power Loads to the Plasma-facing Components in ITER”

This publication presents the first 3D study of fast particle losses in ITER. The ASCOT code was used to assess the risks posed by toroidal field ripple and test blanket modules on the integrity of the first wall. The author performed the ASCOT simulations presented in this paper using input data provided by the coauthors and did most of the data analysis and developed the tools for the visualization of the results. All figures, apart from Figures 5 and 9 were produced by the author. The author co-wrote the paper and the responses to the referees.

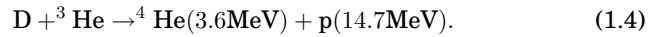
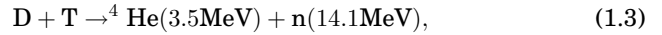
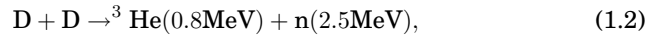
Publication V: “ITER ELM control coils: effect on fast ion losses and edge confinement properties”

This publication studies the consistency of vacuum modelling for ELM control coils in ITER. The ASCOT4 suite was used to calculate 3D magnetic field maps and to perform fast ion loss simulations that pointed out the inconsistencies of this approach. The author co-developed the new code, ASCOT4 with the co-authors of the paper. The author did the calculations for the vacuum error fields with the BioSaw code and performed the field line analysis presented in the paper. The author ran the ASCOT4 simulations to calculate the fast ion losses. The author wrote the full paper and the response to the referees.

1. Introduction

Energy is produced in the sun by nuclear fusion reactions [1]. The energy is transmitted to us via radiation and stored in various forms that we can take advantage of in our daily life. Some of these forms are obvious, such as solar and biomass energy, while others are less so, but virtually all forms of energy available to us originate from fusion in the stars. The idea of utilizing nuclear fusion directly for power production [2] is an enticing one, since it would allow us to extract the energy directly from its source rather than its derived forms.

In a nuclear fusion reaction two light nuclei are fused into a heavier one. In the process, some of the energy stored in the nuclear bonds of the nuclei will be released as kinetic energy of the reaction products. For power production in a reactor, the fusion reactions between the heavy isotopes of hydrogen, deuterium (D) and tritium (T) as well as the light isotope of helium (^3He) are considered feasible. Those reactions can be described by the equations



The rate at which the reactions spontaneously occur is described by atomic cross-sections that are functions of temperature [3], shown in Figure 1.1. At the temperature of 10 keV, the temperature range achievable in today's fusion experiments, the cross-section of the DT reaction (1.3) is the highest by two orders of magnitude. Therefore, it seems certain that fusion reactors of the first generation will operate with DT fuel.

Fusion energy would hold several advantages over conventional methods energy production. The most important advantages are the abun-

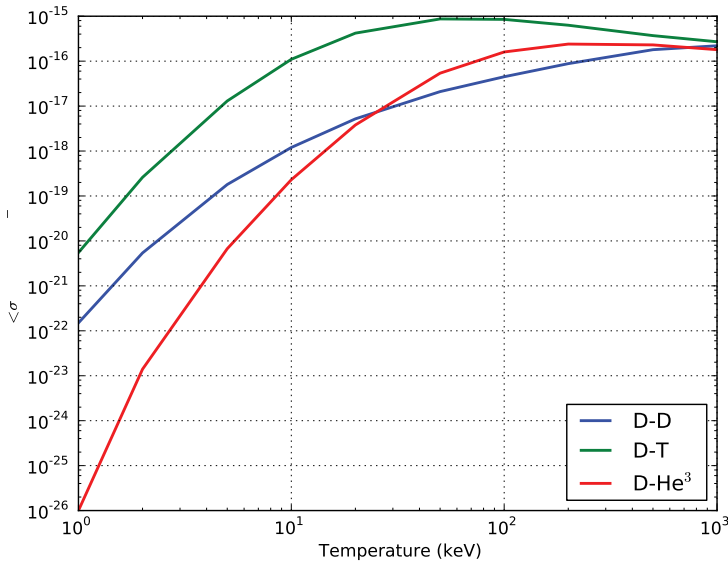
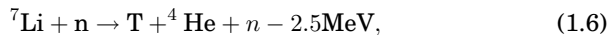


Figure 1.1. Cross-sections of thermal fusion reactions as a function of temperature on a logarithmic scale [3]. The temperatures achievable in man-made devices are currently in the order of 10^1 keV, where the DT reaction has a cross-section two orders of magnitude above the other candidates. Only above 10^3 keV do the other reactions become comparable.

dance of fuel and relatively harmless waste. Deuterium can be extracted from seawater and tritium can be bred in the reactor from the naturally occurring isotopes of lithium by neutron induced fission reactions [4],



utilizing the fast neutrons produced by the fusion reactions (1.2) and (1.3). Both lithium and deuterium are fairly evenly distributed geographically and are unlikely to lead to political conflicts due to scarcity of resources. In addition to neutrons, the fusion reactions produce isotopes of helium and hydrogen that do not contribute to greenhouse emissions. Helium isotopes are radioactively stable and the only radioactive hydrogen isotope, tritium, has a relatively short half-life of 12.3 years and thus does not require the long-term storage necessary for spent nuclear fission fuel. The neutrons released in the fusion reactions cause activation in the reactor, in a manner similar to activation of reactor components in nuclear fission reactors. However, the radioactivity of activated components is typically short-lived if the reactor materials are chosen wisely.

Although fusion reactions release energy, in order to initiate a fusion re-

action the two nuclei have to collide with enough energy to penetrate the the Coulomb repulsion of like charges. In a reactor this requires heating the fuel to high enough temperature for the thermal velocity of the particles to reach this condition. Unfortunately, the required temperature in a fusion reactor is in the order of a hundred million degrees Kelvin, roughly ten times the temperature of the center of the sun. At such high temperature, matter is in plasma state, an ionized gas characterized by electromagnetic interactions. When dealing with high temperatures in plasma physics it is convenient to use the electron volt as a unit of temperature. The conversion to kelvin is approximately $1 \text{ eV} = 11\,600 \text{ K}$.

The requirement for extremely high fuel temperature and a desire to keep the fuel clean of impurities poses a problem for reactor design. Any material surface that comes into contact with the plasma will be eroded and the eroded material will dilute the fusion fuel. Two main approaches to plasma confinement have been pursued since the 1950's, inertial confinement and magnetic confinement. In inertial confinement, pellets of DT fuel are rapidly compressed. The increase of pressure heats the fuel, and fusion occurs in the time it takes for the pellet to fall apart. An inertial confinement reactor might work in a fashion similar to an internal combustion engine. In magnetic confinement, the plasma is suspended in vacuum using a magnetic field and heated by electromagnetic waves and particle beams until a sufficient temperature is reached. A magnetic confinement fusion reactor can, in principle, operate in steady-state using superconducting magnets.

This thesis will discuss issues related to magnetic confinement fusion. A recent review about inertial confinement fusion published by the IAEA can be found in [5, Chapter 10].

1.1 Tokamaks

The most promising design for harnessing nuclear fusion for power production via magnetic confinement is the tokamak [6]. A tokamak is a toroidal vacuum chamber in which plasma can be suspended by a magnetic field. Since toroidal systems are going to be discussed throughout this thesis, it is worthwhile to start with the description of a torus. In geometry, a torus is a surface of revolution generated by revolving a circle about an axis coplanar with the circle. In tokamaks, the radius of revolution, the so-called *major radius* is larger, often much larger, than the

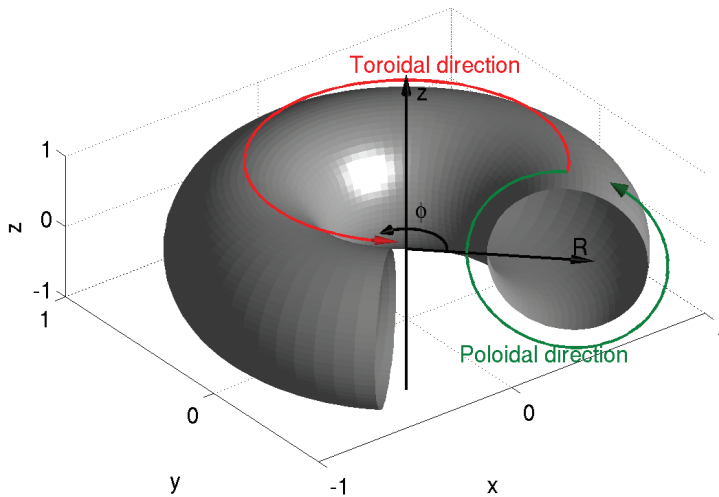


Figure 1.2. The cylindrical coordinate system (R, ϕ, z) commonly used to describe tokamaks. The Cartesian coordinates R and z define the poloidal plane, and the geometric poloidal angle, $\theta = \tan^{-1}(R - R_0/z - z_0)$, is occasionally used. The toroidal angle, ϕ , lies in the plane perpendicular to the poloidal plane and increases counterclockwise when viewed from the top (positive z) of the torus.

radius of the circle, called the *minor radius*. An illustration of such a torus is shown in Figure 1.2. A cylindrical coordinate system (R, ϕ, z) is often used to describe the torus, where R is the major radius, ϕ is the *toroidal* angle and z lies along the axis of revolution. The plane spanned by the R and z coordinates is called the *poloidal* plane, and any vector components in the plane are referred to as poloidal. The direction perpendicular to the poloidal plane, is called the toroidal direction.

The magnetic field of a tokamak is a superposition of a toroidal field that is generated by coils surrounding the vessel, and a poloidal field generated by inducing a toroidal current in the plasma by a current flowing in a central solenoid. The field lines of the equilibrium field have a *helical* structure and they map out cocentric toroidal surfaces of constant magnetic flux as illustrated in Figure 1.3. An equilibrium between the plasma pressure and the magnetic pressure can be found where the plasma is confined by the magnetic field. The equilibrium must satisfy the force balance condition $\mathbf{J} \times \mathbf{B} = -\nabla p$, i.e., the magnetic pressure must balance the kinetic pressure. It follows that $\nabla p \cdot \mathbf{B} = 0$, i.e., the pressure is constant on surfaces of constant magnetic flux. Due to the geometry, the

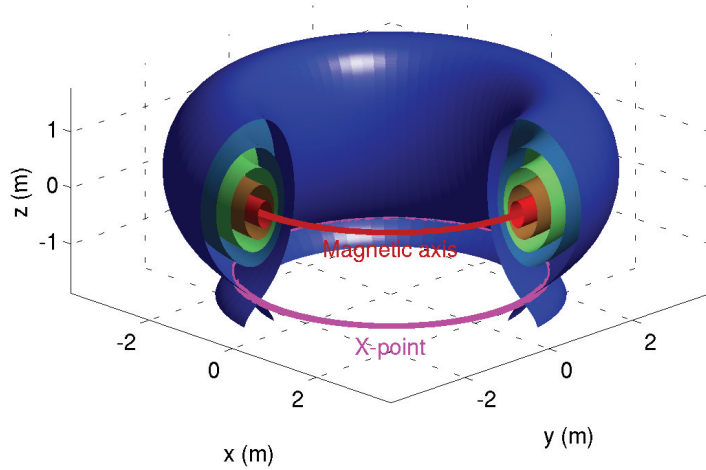


Figure 1.3. Surfaces of constant magnetic flux in the plasma equilibrium in the Joint European Torus (JET) tokamak. Since JET is a divertor tokamak, the equilibrium has an X-point, indicated by the thick purple curve. Above the X-point, the flux surfaces are concentric around the magnetic axis, indicated by the thick red curve. The X-point lies on the Separatrix, colored in dark blue, that separates the hot core plasma from the cold edge plasma.

pressure must have a maximum on the magnetic axis and a gradient only perpendicular to the flux surfaces.

Magnetic flux surfaces in a tokamak are deemed open or closed, based on whether they intersect the vessel walls or not. The closed flux surfaces form the *core plasma* while the open flux surfaces form the edge plasma, which consists of the Scrape-Off Layer (SOL) and its halo plasma, as illustrated in Figure 1.4. The plasma is free to flow rapidly along flux surfaces and hence only the closed flux surfaces are capable of confining the plasma for a significant time. The core and the SOL are separated by a magnetic *separatrix*, generated in most today's tokamaks by a set of coils that create an X-point in a magnetic surface within the vacuum chamber. Although the X-point configuration restricts the core plasma to a smaller volume, the interaction between the plasma and the material surface is limited to a small area where the open flux surfaces closest to the separatrix intersect the vessel, the *divertor* as illustrated in Figure 1.4.

The toroidal *plasma current* also heats the plasma resistively. However, the resistivity of the plasma decreases as a function of electron temperature and non-Ohmic heating methods are required to heat the plasma into

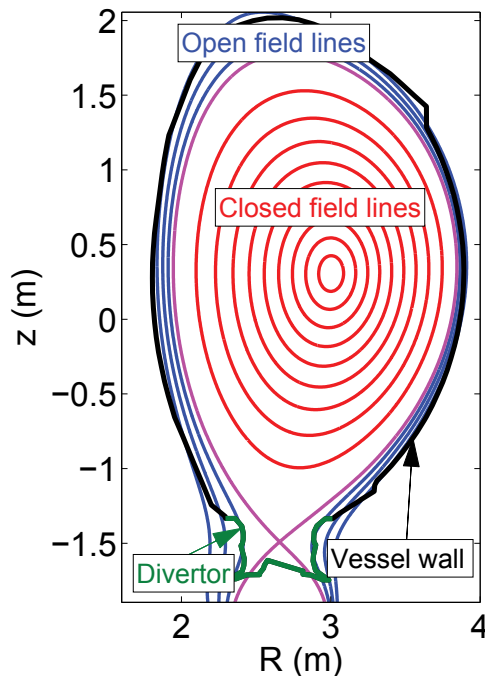


Figure 1.4. The poloidal cross-section of the magnetic equilibrium and the vessel wall in the JET tokamak. The area enclosed by the vacuum chamber, composed of the first wall (black curve) and the divertor (green), is divided into open (blue) and closed (red) field lines, separated by the LCFS (magenta). Open field lines close on themselves within the chamber while open field lines intersect the material surfaces. Most open field lines are guided into the divertor in the bottom part of the vessel where most of the plasma-wall interaction occurs.

fusion-relevant temperatures. Once the sufficient temperature for fusion has been reached, the fusion reactions begin to self-heat the plasma and ignition is achieved when self-heating becomes sufficient to maintain the fusion burn. Both the auxiliary heating methods and the fusion reactions, discussed in more detail in Chapter 2, create a minority population of fast ions within the plasma with a temperature much higher than the bulk plasma temperature. These fast ions remain confined in the magnetic field and slowly heat the main plasma through Coulomb collisions with the bulk plasma ions and electrons.

Heat and particles are free to flow along magnetic flux surfaces, but are constrained from moving across flux surfaces by the magnetic field. However, collisions between particles cause transport perpendicular to the magnetic field. The collisional transport of particles, heat and momentum in tokamaks is described by the so-called *neoclassical* transport theory [7, 8]. Unfortunately, the level of transport observed experimentally in tokamaks tends to drastically exceed the predictions of neoclas-

sical theory. Gradients of temperature and density upheld by external heating and fuelling drive plasma turbulence responsible for most of the observed perpendicular transport [9], often exceeding neoclassical estimates by orders of magnitude [10].

In 1982, experiments at the ASDEX Upgrade tokamak showed that the plasma suddenly enters a mode where a higher pressure can be maintained by the magnetic field when the heating power exceeds a threshold value [11]. In this so-called *H-mode*, turbulence is suppressed at the edge of the confined plasma, for reasons that still are a subject of active research. Plasma pressure builds up a steep gradient in this region of suppressed turbulence, often called the *transport barrier* or the *pedestal*. When the pressure in the pedestal exceeds a threshold value, an instability called an Edge Localized Mode (ELM) occurs [12, 13]. During an ELM, the edge pressure gradient collapses and a substantial fraction of the plasma stored energy is expelled from the core plasma to the Scrape-Off Layer (SOL) whence it rapidly flows to the divertor. ELMs become more severe in larger tokamaks, because the plasma confined energy scales with the plasma volume, proportional to R^3 , while the area into which an ELM deposits its energy only scales with R , the linear size of the machine. Therefore, larger tokamaks will invariably have larger transient heat loads from ELMs and, unfortunately, we are already at the tolerance limit of divertor materials. The ELM cycle is typical of H-mode plasmas and since it is, on the other hand, needed for impurity purging, it has to be fully understood before tokamak fusion reactors can be operated.

The tokamak design is entering its final experimental phase in the upcoming decade when the construction of ITER, an international tokamak reactor, is finished in Cadarache, France [14]. ITER will be the first tokamak experiment to, among other things, demonstrate net power production by nuclear fusion. A schematic view of ITER is shown in Figure 1.5.

1.2 New physics explored in ITER

It is often said that the remaining issues for fusion energy are related to technology and design, the durability of reactor materials being the most prominent one, but this is not entirely true. While the technical challenges in confining a burning plasma over the lifetime of a reactor are not to be disregarded, the approaching operation of ITER will also

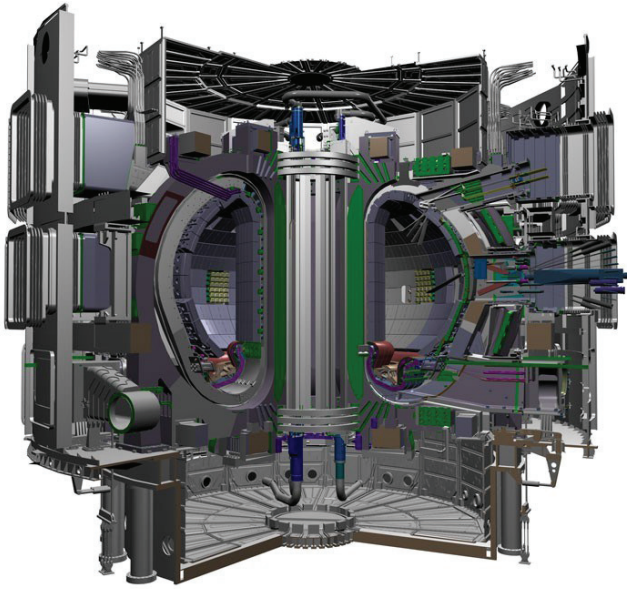


Figure 1.5. A cut-open view of the ITER tokamak. The major radius is approximately 6 m, the minor radius 2 m and the whole machine is nearly 30 m tall. ©ITER organization

present us with new physics that has not been encountered in today's experiments.

The confinement of the 3.5 MeV alpha (^4He) particles from DT fusion is crucial for ITER. The majority of alpha particles must deposit their energy to the thermal plasma to sustain the temperature required by the fusion burn. Furthermore, even small alpha particle losses ($\sim 1\%$), concentrated on a small wall surface area, are sufficient to expose the plasma facing first wall components to unacceptable heat loads [15], risking melting and erosion. On the other hand, thermalized alpha particles, so-called *helium ash*, must be flushed out of the plasma to avoid dilution of the hydrogenic fuel. Alpha particles are born in thermal fusion reactions deep in the core plasma, and the understanding of their transport towards the cold edge plasma is the key to controlling the fusion burn. Prior knowledge of fusion alpha particle physics comes from D-T experiments on TFTR [16] and JET [17] in the 1990's, which produced the highest controlled fusion power on record. In these experiments, alpha particle losses were found to be small ($< 5\%$) when the machines were operated with a high plasma current, as is the case in ITER. However, analysis of fast ion loss detector data at TFTR identified the dominant loss mechanism as the toroidal

field (TF) ripple [18], a periodic variation in the magnetic field that can give rise to localized losses on lightly shielded wall tiles. TF ripple is an intrinsic feature of tokamaks that will be discussed in more detail in 2.2.1 and will also be present in ITER. The simulation tools and computing resources available in the 1990's were not capable of accurately modelling the heat loads due to ripple losses on the plasma facing components and, hence, extrapolations to ITER could not be immediately made. What is required is a Monte Carlo code that takes into account “the detailed 3-D geometry of the outer magnetic flux surfaces and the tokamak first wall” and the effect of “the finite gyroradii of the fast ions” [18]. The development of Monte Carlo codes, and the increase of computing power available to fusion research has now made such studies possible.

The accumulation of helium ash is kept in control by the ELMs that periodically flush heat and particles from the cold edge plasma to the divertor. However, according to scaling laws, the natural ELMs in ITER are predicted to deposit roughly 10 MJ of energy on a 10 m^2 area of the divertor in less than 1 ms at a frequency of a few Hz [19, 20], which is unsustainable for any known divertor material. The ELMs are a necessity but their frequency and amplitude must be controlled in order to operate ITER beyond the first few plasmas [21]. A number of ELM control techniques have been developed [22] and the most promising one seems to be the perturbation of the pedestal magnetic field with a 3D error field generated by in-vessel coils [23–25]. Understanding has been acquired of the effect of external magnetic perturbations on plasma confinement and transport [26], but the interplay of the magnetic perturbations with the fast ion population raises the concern of localized losses. Similarly to TF ripple losses, the losses due to external coils have to be simulated with state-of-the-art Monte Carlo codes in order to make accurate predictions for ITER.

1.3 Scope of the thesis

The aim of this thesis is to reliably model the effect of the 3D magnetic geometry on the confinement and losses of fast ions in ITER. The work consists of numerical simulations in realistic tokamak 3D geometry with the kinetic Monte Carlo code ASCOT [27–29], developed at Aalto University and the VTT Technical Research Centre of Finland since the 1990s. In recent years, the ASCOT code has been developed by the group at Aalto

University into a very suitable tool for carrying out massive fast ion simulations in realistic 3D geometries. In this thesis, the latest developments of ASCOT have been applied to simulations of fast ions in ITER, as well as in several existing tokamaks. Two key questions are addressed: First, does ASCOT correctly capture the essential physics of fast ions? The answer to this question requires validation of ASCOT with established codes in the fusion community and experimental results. Second, once ASCOT has been sufficiently validated, are fast ion losses going to be a problem in ITER, and how can they be avoided?

The thesis is organized as follows: In Chapter 2, the equations that determine the motion of charged particles in magnetic fields are introduced. The collisionless orbits of charged particles in axisymmetric tokamak geometry are described, and the effect of collisions with the background plasma in the single-particle picture is discussed. The magnetic perturbations that typically break the axisymmetry in real tokamaks are then introduced, and the present knowledge about their effect on fast ion losses is discussed. In Chapter 3 the modelling tools used in this work and the tokamaks that have been studied are described. The limitations of fast ion diagnostics are also briefly discussed to highlight the importance of fast ion modelling. The main features and developments of the ASCOT code relevant for this work are discussed in detail. Finally, the JINTRAC suite of codes that can be interfaced to ASCOT for self-consistent plasma transport simulations is also introduced. In Chapter 4, two main sets of modelling results are presented: Publications I, II and III describe studies performed on existing tokamaks, where ASCOT results have been validated with experimental measurements. Publications IV and V then describe predictive ASCOT modelling of fast ion losses due to various 3D magnetic perturbations expected in ITER. Finally, a summary, the main conclusions and some future prospects are given in Chapter 5.

2. Fast Ions in Tokamak Environment

Fast ions are ions whose energy is at least an order of magnitude above the thermal energy of the plasma. Fast ions are externally introduced into the tokamak plasma, mostly to heat the plasma beyond the limits of Ohmic heating. Understanding the physics of fast ions is important because although their concentration is typically small ($\sim 1\%$), they may carry as much as half the energy in a tokamak plasma. Confinement of fast ions is extremely important for the heating efficiency and the lifetime of structural components of the tokamak. Fast ions transfer energy slowly to the main plasma through collisions with thermal electrons and ions over their slowing-down time, which is of the order of 1 s for alpha particles in ITER. Fast particles that are lost before transferring all their energy to the plasma cause degradation of the heating efficiency. Furthermore, fast ion losses can cause significant structural damage to the plasma facing components of the tokamak by melting or eroding material surfaces [15]. On the other hand, thermalized non-hydrogenic fast ions, such as alpha particles, must be flushed out to avoid dilution of the hydrogen fuel. There are three main sources of fast ions commonly encountered in today's tokamaks: Neutral Beam Injection (NBI), Ion Cyclotron Resonance Heating (ICRH), and internal fusion reactions.

In NBI heating, charged particles are accelerated in a particle accelerator and then neutralized before being injected into the plasma [30]. Electrically neutral fast particles can penetrate the magnetic field until they are re-ionized when they come into contact with the hot plasma. The energy of the beam particles must be sufficient to reach the plasma center, but low enough to avoid so-called “shine-through”, i.e., passing through the plasma unionized. In most experiments today, NBI ions are accelerated to energies of the order 100 keV. ITER is a much larger machine and the plan is to use 1 MeV neutral beams to ensure that the beam heating

reaches the plasma center. Neutral beam ions are typically H, D or T ions, since hydrogenic ions do not dilute the plasma and even contribute to fuelling [31]. However, hydrogenic beams always contain small fractions of particles with $1/2$ and $1/3$ of the nominal acceleration energy. Some of the charged particles in the accelerator form molecular ions (H_2^+ , H_3^+) with a lower charge/mass ratio to the atomic ions. When the accelerated molecular ions break up in the plasma, the remaining ions are left with a $1/M$ fraction of the nominal energy, where M is the mass number of the molecule.

In ICRH heating, radio waves at a harmonic frequency of the ion cyclotron frequency $\Omega = ZeB/m$ are injected into the plasma, accelerating ions that are in resonance with the wave electric field [32]. Since in tokamaks $B \sim 1/R$, all ions of the same charge to mass ratio will be accelerated when they pass the resonance radius. However, waves at the cyclotron frequency of the main plasma ions cannot propagate into the plasma and a different frequency must be chosen. The most common scheme is to heat a minority ion species in the plasma with a different charge to mass ratio, for example H or ^3He in a D plasma, and transfer the energy to the main plasma via collisions. Since more energetic ions become less collisional, their energy can keep growing as they make more passes through the resonance layer between collisions. ICRH heated ions can reach an energy of several MeV even in today's experiments.

Fusion reactions in today's tokamaks predominantly occur between fast ions generated by NBI or ICRH and thermal plasma ions. Due to radiation safety, tritium is very rarely used and most experiments are carried out with pure deuterium plasmas, some even with plain hydrogen. The thermal DD fusion cross-section is very low, but the fast deuterium ions can access higher cross-sections and produce DD fusion reactions. DD fusion can produce either 1 MeV tritium or 800 keV helium-3 ions (recall Equations (1.1) and (1.2)). In ITER and future fusion reactors, the dominant fusion source will be thermal DT fusion, which produces 3.5 MeV alpha particles, recall Equation (1.3). Fusion products are typically born at the center of the plasma, where the temperature and density are highest, with an isotropic velocity distribution.

In this chapter the fundamental theory required to understand fast ion dynamics in a tokamak geometry is presented. First, in Section 2.1 the equations of motion of fast ions in slowly varying magnetic and electric fields are presented. Unperturbed particle orbits in the tokamak geome-

try are discussed in Section 2.1.1, and perturbations due to interactions with the thermal plasma are discussed in Section 2.1.2. In Section 2.2 the most common static magnetic perturbations encountered in tokamaks are introduced and their effect on fast ion confinement is discussed.

2.1 Fast ion motion

The motion of charged particles in electric and magnetic fields is governed by the Lorentz force

$$m\ddot{\mathbf{r}} = Ze(\mathbf{E} + \dot{\mathbf{r}} \times \mathbf{B}), \quad (2.1)$$

where m is the mass of the particle, Z is the charge number of the particle, e is the unit charge, \mathbf{r} is the position of the particle, $\dot{\mathbf{r}} = \mathbf{v}$ is the velocity of the particle, \mathbf{E} is the electric field, and \mathbf{B} is the magnetic field. In the absence of an electric field, the force on the right hand side of Equation (2.1) is always perpendicular to both the velocity of the particle and the magnetic field, which results in *gyromotion* around magnetic field lines. The radius of the gyration, the so-called Larmor radius $r_L = mv_\perp/(ZeB) = v_\perp/\Omega$ [4], where v_\perp is the component of \mathbf{v} perpendicular to the magnetic field, and $\Omega = ZeB/m$ is the gyrofrequency. Since the magnetic force is always perpendicular to \mathbf{v} , the magnetic field does no work on the particle but only acts on the direction of its velocity.

It is often convenient to separate the fast periodic gyromotion from the motion of the center of gyration, the so-called *guiding centre*, by writing

$$\mathbf{r} = \mathbf{r}_{GC} + \mathbf{r}_L. \quad (2.2)$$

The vector $\mathbf{r}_L = \hat{\mathbf{b}} \times \mathbf{v}/\Omega$ points from the guiding center to the position of the particle on the gyro-orbit and it averages to 0 over the period of the gyromotion if the gradient length of the magnetic field is much larger than r_L . To understand the dynamics of guiding-center motion, it is sufficient to calculate an approximate solution to Equation (2.1) using Newtonian mechanics. Inserting Equation (2.2) into Equation (2.1), expanding the fields around \mathbf{r} , and solving it to first order in $\epsilon' = m/(Ze)$ yields

$$\ddot{\mathbf{r}}_{GC} + \ddot{\mathbf{r}}_L = \frac{1}{\epsilon'} [\mathbf{E} + (\mathbf{r}_L \cdot \nabla) \mathbf{E} + (\mathbf{r}_{GC} + \mathbf{r}_L) \times (\mathbf{B} + (\mathbf{r}_L \cdot \nabla) \mathbf{B})] + \mathcal{O}(\epsilon'). \quad (2.3)$$

With some vector algebra [33, 34], Equation (2.3) can be averaged over the phase of the gyration to obtain an equation of motion for the guiding center,

$$\ddot{\mathbf{r}}_{GC} = \frac{1}{\epsilon'} \left(\mathbf{E} + \dot{\mathbf{r}}_{GC} \times \mathbf{B} - \frac{\mu}{Ze} \nabla B \right) + \mathcal{O}(\epsilon'), \quad (2.4)$$

where $\mu = \frac{mv_{\perp}^2}{2B}$ is the magnetic moment, an adiabatic invariant of the motion. The fields \mathbf{E} and \mathbf{B} in Equation (2.4) are evaluated at \mathbf{r}_{GC} . The motion of the guiding center consists of *parallel motion* with velocity $v_{\parallel} \hat{\mathbf{b}}$ along the magnetic field, and *drift motion* with velocity \mathbf{v}_D perpendicular to the magnetic field.

The parallel motion of the guiding center is obtained by solving the parallel component of Equation (2.4), which yields

$$\dot{v}_{\parallel} = \frac{1}{\epsilon'} \left(E_{\parallel} - \frac{\mu}{Ze} \nabla_{\parallel} B \right). \quad (2.5)$$

The second term in Equation (2.5) is the *magnetic mirror force* that plays an important part on the motion of particles in tokamaks. It will be revisited in more detail in the next section.

The drift velocity of the guiding center is obtained by solving the perpendicular component of Equation (2.4) and writing out the total time derivative $\dot{\mathbf{r}}_{GC}$. After some algebra [33, 34], one arrives at

$$\begin{aligned} \mathbf{v}_D = & \frac{\mathbf{E} \times \mathbf{B}}{B^2} + \frac{W_{\perp}}{ZeB^3} \nabla B \times \mathbf{B} + \frac{2W_{\parallel}}{ZeB^3} \mathbf{B} \times (\mathbf{b} \cdot \nabla) \mathbf{B} \\ & + \frac{mv_{\parallel}}{ZeB^2} \mathbf{B} \times (\mathbf{u}_E \cdot \nabla) \mathbf{b} + \frac{mv_{\parallel}}{ZeB^2} \mathbf{B} \times \partial_t \mathbf{b} + \frac{m}{ZeB^2} \mathbf{B} \times \dot{\mathbf{u}}_E + \mathcal{O}(\epsilon') \end{aligned} \quad (2.6)$$

The first term is the $\mathbf{E} \times \mathbf{B}$ drift velocity \mathbf{u}_E and the second and third terms are the magnetic *gradient* and *curvature* drifts. The $\mathbf{E} \times \mathbf{B}$ drift arises from acceleration and deceleration during the gyro-orbit due to an electric field. It is independent of electric charge ,i.e., electrons and ions drift in the same direction. The gradient and curvature drifts stem from the nonuniformity of the magnetic field during the gyro-orbit. The gradient drift arises from small changes in the Larmor radius during the gyro-orbit, and the curvature drift arises from inertia of the parallel motion along curved field lines. Both the gradient and curvature drifts depend on the charge and will separate positive and negative charges. Only the first three terms are significant in stationary fields and weak electric fields, the rest are often neglected. The last term of Equation (2.6) is often referred to as the *polarization drift* and it becomes significant when addressing plasma turbulence.

Equation (2.4) is only accurate to first order in ϵ' . It is sufficient for understanding the physics of charged particle motion, but for numerical applications the equations must be solved to greater accuracy. This is possible when the equations of motion are derived in the Hamiltonian formalism. Instead of gyroaveraging the equation of motion to order ϵ' , the Lagrangian of a charged particle [35] is gyroaveraged, and the equations

of motion in $\mathbf{r}_{GC}, p_{\parallel}, \mu, \theta_g, t$ are solved from the Euler-Lagrange equation, where the velocity space coordinates have been chosen as the parallel momentum p_{\parallel} , the magnetic moment μ and the gyrophase θ_g . The solution is accurate to all orders in ϵ' [33, 36] because of the Hamiltonian nature of the equations is preserved. Also including even the relativistic effects yields a set of equations for the phase-space coordinates of the guiding center [37]

$$\begin{aligned}\dot{\mathbf{r}}_{GC} &= \frac{p_{\parallel}}{\gamma m} \frac{\mathbf{B}^*}{B_{\parallel}^*} + \epsilon' \mathbf{E}^* \times \frac{c \mathbf{b}}{B_{\parallel}^*} \\ \dot{p}_{\parallel} &= Ze \mathbf{E}^* \cdot \frac{\mathbf{B}^*}{B_{\parallel}^*} \\ \dot{\mu} &= 0 \\ \dot{\theta} &= \frac{1}{\epsilon'} \frac{ZeB}{\gamma mc},\end{aligned}\tag{2.7}$$

where c is the speed of light and $\gamma = \sqrt{1 + (p/mc)^2}$ is the relativistic Lorentz factor. In these equations, the fields \mathbf{E} and \mathbf{B} have been replaced by the effective fields

$$\begin{aligned}\mathbf{B}^* &= \nabla \times \mathbf{A}^* \\ \mathbf{E}^* &= -\frac{1}{c} \frac{\partial \mathbf{A}^*}{\partial t} - \nabla \Phi^*\end{aligned}\tag{2.8}$$

and the potentials \mathbf{A} and Φ by the effective potentials

$$\begin{aligned}\mathbf{A}^* &= \mathbf{A} + \frac{mc}{\epsilon' Ze} \gamma v_{\parallel} \hat{\mathbf{b}} \\ \Phi^* &= \Phi + \frac{mc}{Ze} \gamma c\end{aligned}\tag{2.9}$$

The details of the Hamiltonian derivation can be found in many sources in literature, such as [8, 33, 34, 38] and will not be discussed here.

2.1.1 Collisionless orbits in toroidal geometry

Due to the toroidal geometry, there is a magnetic field gradient towards the center of the torus and a curvature of the field lines, which gives rise to a drift velocity, the so-called ∇B drift, in the vertical (z) direction. Usually the direction of the tokamak magnetic field is set up in such a way that the direction of the drift is towards the divertor. To prevent the separation of charges due to the ∇B drift, the magnetic field of a tokamak has a poloidal component and the total field is *helical*. As charged particles circulate around the torus, the ∇B drift deviates them from their initial flux surfaces. However, due to the helicity of the field, the drifts

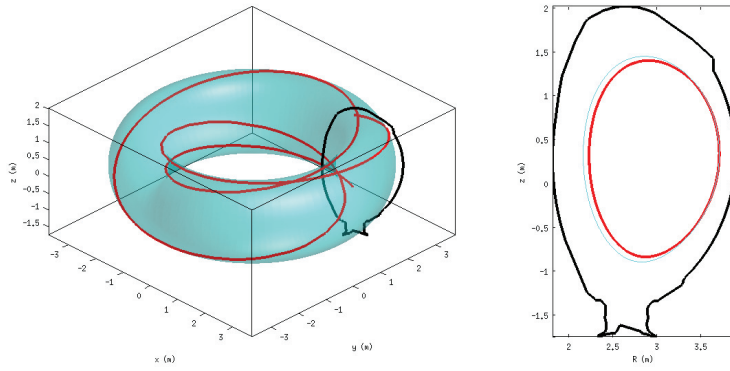


Figure 2.1. A passing guiding-center orbit of a 100 keV NBI ion in the JET tokamak, depicted by the red trace. The orbit is drawn in 3D cartesian space on the left panel, and on the right it is projected into the poloidal cross-section of the torus. The magnetic flux surface on which the particle is born is shown in light blue and the particle deviates from it over the course of the orbit. The outline of the vessel wall and the divertor is displayed by the black curve.

cancel over one poloidal circuit in an axisymmetric geometry, and the particles remain confined on closed orbits. The majority of charged particle orbits can be categorized into *trapped* or *passing* orbits. For simplicity we neglect electric fields here.

Passing orbits circle the poloidal cross-section of the tokamak, as illustrated in Figure 2.1. In the absence of electric fields, the ∇B drift deviates the particle radially inward in the upper hemisphere of the poloidal cross-section and outward in the lower hemisphere. In axisymmetric geometry, the drifts cancel out over a complete poloidal orbit and passing orbits close on themselves in the poloidal plane. In real space, a passing orbit maps out a toroidal drift surface.

Particles can become trapped on the low field side (LFS) of the magnetic field, on orbits such as the one shown in Figure 2.2. Trapping can be best understood in terms of conservation of energy and magnetic moment. The kinetic energy of a particle can be written as $W = \frac{1}{2}mv_{\parallel}^2 + \mu B$. When the particle moves towards a higher magnetic field, its parallel velocity must decrease to conserve W and μ . If the magnetic field reaches the value W/μ along the orbit, it follows that $v_{\parallel} = 0$ and the particle cannot propagate to any higher B . Because of the parallel acceleration proportional to $-\nabla B$ in Equation (2.5), the particle is then reflected back toward the outboard side. Since the particle spends a relatively long time near the reflection points where its parallel velocity is close to 0, the ∇B drift deviates it further from its original field line over one orbit than a passing particle.

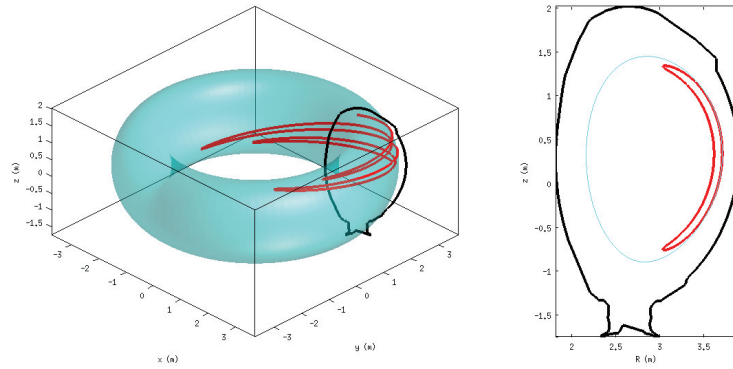


Figure 2.2. A trapped guiding-center orbit of a 100 keV NBI ion in the JET tokamak, depicted by the red trace. The orbit is drawn in 3D cartesian space on the left panel, and on the right it is projected into the poloidal cross-section of the torus. The magnetic flux surface on which the particle is born is shown in light blue. The outline of the vessel wall and the divertor is displayed by the black curve.

Upon returning to the outer midplane, trapped orbits have a finite width that is proportional to $\epsilon^{1/2} r_{L,p}$ [8], where $r_{L,p} = mv_{\perp}/(ZeB_p)$ and $\epsilon = r/R$ is the inverse aspect ratio. The finite width gives the orbit a distinctive shape in the poloidal cross-section that resembles a banana, hence the commonly used name *banana orbit*. In axisymmetric geometry, banana orbits are also close upon themselves in the poloidal plane. In real space, banana orbits undergo a precession motion around the torus, due to the shorter length of the return leg of the orbit.

In addition to passing and trapped orbits, there are more exotic orbit types, such as orbits on the trapped-passing boundary and orbits where the parallel motion is dominated by the drift motion. A good review of orbits can be found in [39]. However, for this work such exotic orbits do not play an important role.

2.1.2 Interactions in a plasma

The motion of charged particles outlined in the previous sections is strictly speaking only true in vacuum. A charged particle moving in a plasma undergoes a random walk in velocity space due to Coulomb collisions with other particles inside its Debye sphere, which causes cross-field transport. Although the particle experiences a continuum of small deflections, it is often convenient to treat the collective Coulomb interactions as the cumulative effect of many small binary collisions. Many textbooks define

a $\pi/2$ collision frequency ν and mean free path, which correspond to the time and distance over which the velocity of the particle is deflected by an angle of $\pi/2$.

If one considers the guiding center approximation discussed in Section 2.1, the position and velocity of the particle deterministically define the position of the guiding center by $\mathbf{r}_{GC} = \mathbf{r} + (\mathbf{v} \times \mathbf{b})/\Omega$. Therefore, a deflection of \mathbf{v} by π will displace the guiding center by a distance $2v_{\perp}/\Omega$. The direction of the displacements depends on the gyrophase of the particle and can be considered random in the guiding center approximation. The flux of particles across the magnetic field due to the random displacements can be described by diffusion, $\Gamma = -D\nabla n$. The diffusion coefficient D is proportional to the collision frequency ν and the square of the step size of the random walk, r_L . The diffusion coefficient for cross-field classical transport is therefore $D \sim \nu r_L^2$. This is known as *classical transport*.

Particle trapping in toroidal geometry, discussed in Section 2.1.1, introduces another transport mechanism with a larger step size. When a particle is deflected from a trapped orbit to a passing orbit, its orbit-averaged position will shift radially by the banana orbit width. Therefore, particles close to the trapped-passing boundary will experience large displacements due to collisions. This is known as *neoclassical transport*. Although the fraction of marginally trapped particles is small, the random walk step size and the collision frequency are both large compared to the classical ones. The neoclassical cross-field diffusion coefficient is larger than the classical estimate by a factor $\sqrt{2\epsilon}(B/B_p)^2$ [8], by an order of magnitude in typical tokamaks.

As was pointed out in Section 1.1, experiments in tokamaks routinely observe rates of thermal particle transport that exceed neoclassical estimates by up to two orders of magnitude [10]. It is well established that this *anomalous transport* is caused by turbulent fluctuations driven by gradients in the plasma (See e.g., Ref [9] and references therein). Fortunately, the wide orbits of fast ions tend to average over the turbulent fields and remain mostly unaffected by the plasma turbulence. There is both experimental evidence [15], as well as theoretical work [40, 41] indicating that the transport of fast ions is predominantly neoclassical.

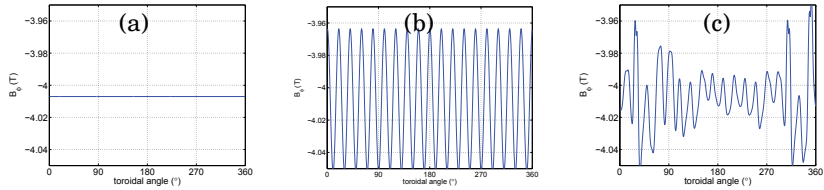


Figure 2.3. The results of different approximations for the toroidal field strength over one toroidal transit in the ITER 15 MA scenario, at the outboard midplane. Figure (a) shows the field strength assuming axisymmetry (toroidally constant field). Figure (b) shows the field strength assuming a harmonic toroidal field ripple due to the gaps between the 18 toroidal field coils. Figure (c) shows the most realistic calculation available to date, taking into account the magnetization of ferritic components and asymmetric coil currents in the machine.

2.2 The breaking of axisymmetry in tokamaks

Ideally, tokamaks are meant to be axisymmetric; the magnetic field and the plasma pressure are designed to be independent of ϕ . The axisymmetry of the magnetic equilibrium is achieved by distributing the field coils uniformly and generating the poloidal field inductively. In reality, the assumption of axisymmetry holds to various degrees in different tokamaks and in many present-day experiments it is intentionally perturbed. In this section, the most important sources for the breaking of magnetic axisymmetry in tokamaks and their impact in ITER are discussed. Figure 2.3 shows the vacuum modelling of the toroidal magnetic field strength along a toroidal circuit of ITER. It gives an indication of the individual magnitudes of the perturbations discussed in this section and the complexity of their combined effect on the axisymmetric magnetic field.

2.2.1 Toroidal field ripple

Toroidal field ripple is a sinusoidal perturbation of the toroidal magnetic field (TF) due to the finite number of TF coils. Since the magnetic field strength decreases with the square of the distance from the coil, the toroidal field has a minimum between two adjacent coils and a maximum at each coil and, therefore, magnetic flux surfaces will have a sausage-like toroidal shape, bulging out between the TF coils. In the large aspect-ratio, ($\epsilon \ll 1$), circular poloidal cross-section approximation, the rippled toroidal field can be expressed as [4]

$$B = B_0 (1 - \epsilon \cos \theta - \delta \sin(N_c \phi)), \quad (2.10)$$

where B_0 is the axisymmetric magnetic field, ϵ is the inverse aspect ratio and N_c is the number of toroidal field coils. The magnitude of the ripple is denoted by δ and it is normally defined as

$$\delta = \frac{B_t^{max} - B_t^{min}}{B_t^{max} + B_t^{min}}. \quad (2.11)$$

The ripple magnitude is a function of R and z , but typically the maximum value along the separatrix, which lies near the outboard midplane, is quoted for a tokamak. The magnitude of δ is a unique parameter for every tokamak, ranging from negligible 0.08 % JET, a large tokamak with 32 coils, up to 7 % in FT-2, a small tokamak with 24 coils.

The ripple perturbs the orbits of trapped particles, which can be understood by analytic theory in simplified geometry [42, 43]. There are two main mechanisms for ripple transport: Ripple-well trapping and stochasticization of banana orbits.

In ripple-well trapping, particles with very low pitch, $\xi = v_{\parallel}/v$, become toroidally trapped in the local minimum of the magnetic field between two adjacent toroidal field coils. The vertical drifts do not cancel along a locally trapped orbit, and ripple-well trapped particles experience a rapid net drift. Therefore, unless they exit the ripple well region or become de-trapped via collisions, they are rapidly lost from the confined plasma. Ripple well trapping occurs when the ripple is strong enough to overcome the $1/R$ dependence of the magnetic field and create local minima of magnetic field strength along a field line. An example of the formation of ripple wells is shown in Figure 2.4. An analytic estimate for ripple well trapping can be calculated in simplified geometry [42]

$$\delta > \frac{\epsilon}{N_c q} |\sin \theta_t|, \quad (2.12)$$

where θ_t is the poloidal angle of the banana orbit turning point and $q = d\phi/d\theta$ is the safety factor. An example of the ripple well region for the natural ripple in the ITER 15 MA standard operating scenario is illustrated in Figure 2.5(a).

Stochasticization of banana orbits is a more subtle effect. The turning points of a banana orbit are located where $\mu B = \frac{1}{2}mv^2$, i.e. the velocity of the particle is completely perpendicular to the magnetic field. Since with finite ripple $B = B(\phi)$, the poloidal position of the turning point will depend on ϕ , which manifests as radial displacements of the orbit. If the radial displacement is large enough to change the toroidal position of the turning point by a significant fraction of the ripple phase, the subsequent

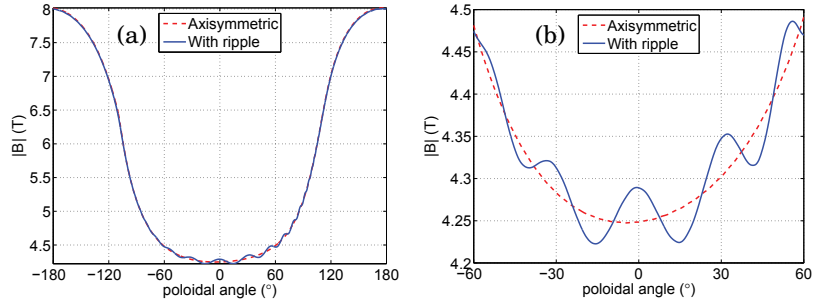


Figure 2.4. The magnetic field strength along the separatrix in the ITER 15 MA operating scenario with the magnetic field ripple due to the 18 discrete coils (a). A blow-up around 0° where the ripple is at its strongest (b). The poloidal angle is equal to 0° on the outer midplane and increases counter-clockwise around the magnetic axis.

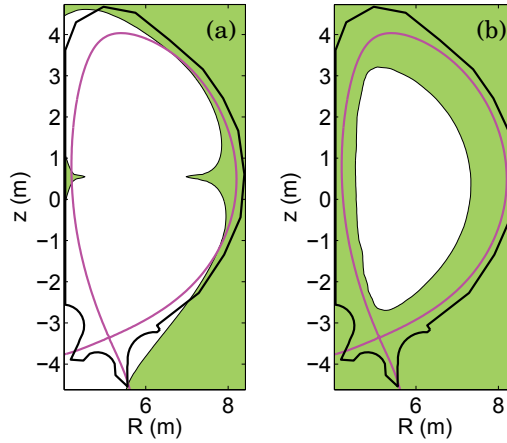


Figure 2.5. Analytic estimates for the ripple loss regions for (a) well trapping and (b) stochastic diffusion of 3.5 MeV alpha particles in the ITER 15 MA operating scenario, indicated by the area shaded in green. Alpha particles on banana orbits with turning points in the loss region will be rapidly lost due to the ripple.

turning point positions become decorrelated and the orbit begins to diffuse, leading to a stochastic transport of trapped particles. The condition for the diffusion has been calculated analytically in a simplified geometry [42]

$$\delta \geq \left[\left(\frac{\pi N q}{\epsilon} \right)^{\frac{3}{2}} r_L \frac{dq}{dr} \right]^{-1}. \quad (2.13)$$

The stochastic diffusion condition thus depends on the position of the particle in both real and velocity space. In real space, the region of stochastic ripple diffusion is typically wider than the ripple well region. Strongly trapped particles, i.e. particles with banana tips close to the outer mid-plane, with high energy are the most susceptible to stochastic ripple diffusion. As an example, the stochastic diffusion region for 3.5 MeV alpha particles in ITER uncompensated ripple is shown in Figure 2.5(b). The stochastization of banana orbits also occurs if the turning points become decorrelated by any other mechanism, such as pitch angle scattering by Coulomb collisions. Therefore, the ripple will enhance the transport of all trapped particles, regardless of whether their Larmor radius fulfils Equation (2.13).

Ripple losses of fast ions have been studied in variable ripple experiments at JET [44], where the ASCOT code was used for safety analysis and predictive modelling. Hot spots caused by localized losses due to ripple wells were identified and also observed in the experiments. Predictions of ripple losses for ITER have been calculated with the ASCOT code and reported in Publication IV. The ripple well region in ITER was found to be too narrow to cause significant losses, and no significant hot spots were predicted. The stochastic diffusion, however, has been identified as a serious risk for fast ion confinement and plans to mitigate the ripple with ferritic inserts are in place. This is further described in the next section.

2.2.2 Magnetized components

It is usually undesirable to introduce ferromagnetic materials into tokamaks, since they will become magnetized and locally reduce the external magnetic field. However, there are situations where the use of ferromagnetic materials can not be avoided or can even be utilized to beneficial effect, e.g., mitigating toroidal field ripple. Experiments in JT-60U have showed that ferritic inserts can be used to reduce the toroidal field ripple [45]. This has been welcome news for ITER [46] whose high intrinsic ripple was predicted to cause problems in Publication IV. Ferritic in-

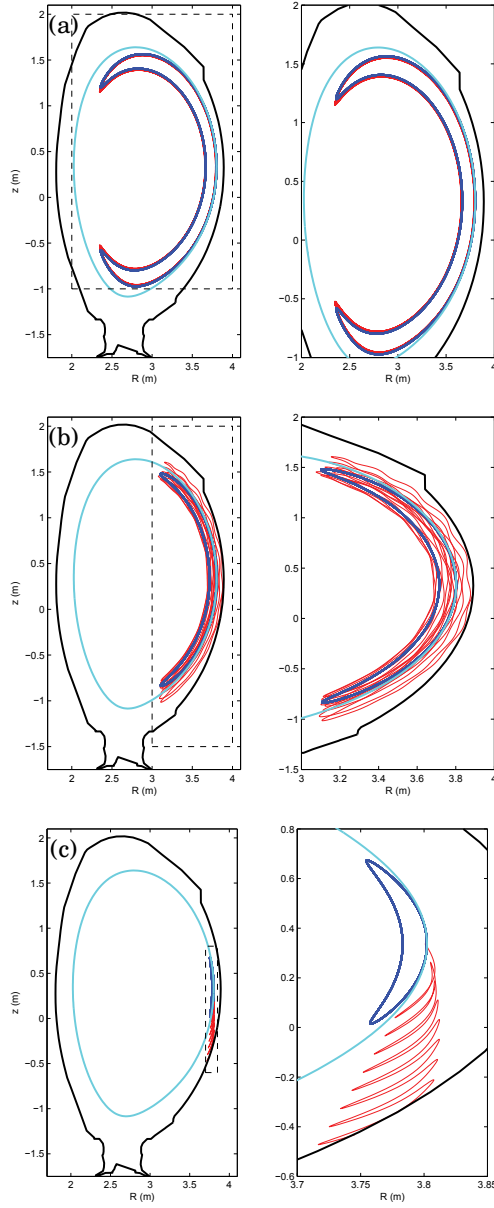


Figure 2.6. The orbits of three trapped 100 keV NBI ions in the JET tokamak with the greatest achievable TF ripple (red trace) and without TF ripple (blue trace), calculated by ASCOT. The ions are initialized at $\rho = 0.95$ (indicated by the light blue curve) on banana orbits opening inward with initial pitch $\xi_0 = 0.6$ **(a)**, $\xi_0 = 0.4$ **(b)** and $\xi_0 = 0.05$ **(c)**. The panels on the right are zoomed to the region indicated by the dashed black line. The first orbit **(a)** has its bounce points outside the ripple loss regions, the second one **(b)** in the stochastic loss region and the third one **(c)** in the ripple well region.

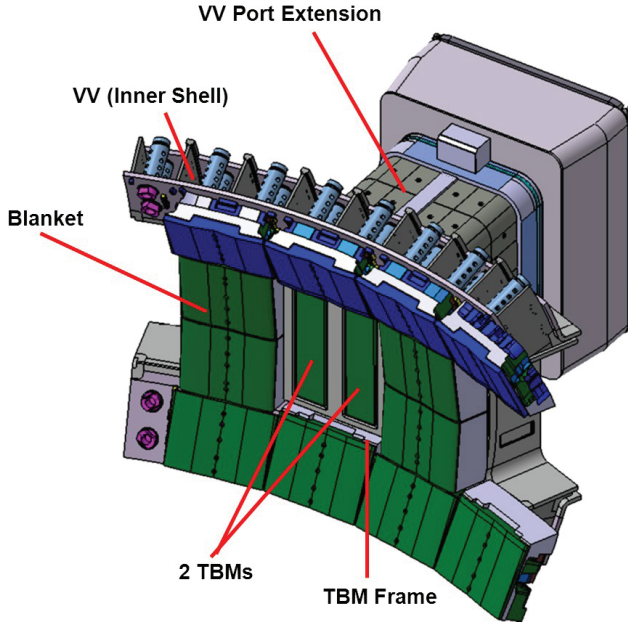


Figure 2.7. The layout of two TBMs in a vacuum vessel (VV) port plug connected to the plasma-facing first wall blanket of ITER. Three of the total of 18 equatorial port plugs in ITER contain a pair of TBMs each. ©ITER organization

serts similar to the ones at JT-60U have now been designed for ITER [47].

In a reactor operating a burning DT plasma, the neutron irradiation will render many materials used in today's tokamaks unsuitable for prolonged use. Ferritic martensitic steels have the least known displacements per atom in neutron irradiation [48] and, therefore, must be used in some of the most critical components. In ITER, a particular hazard is caused by the Test Blanket Modules (TBMs) designed for testing in-situ breeding of tritium from lithium according to the reactions in Equation (1.5) and Equation (1.6). A total of six TBMs are being designed [49] by the ITER partners and they will be installed in pairs in three equatorial port plugs as illustrated in figure 2.7. Each TBM is designed to contain a ton of ferritic steel [50] and will create a localized magnetic perturbation of $\Delta B/B \approx 1\%$ on the last closed flux surface [51].

Local magnetic perturbations change the topology of the magnetic flux surfaces globally [52]. The TBMs locally bend the magnetic field lines outward, but a much more striking feature is the appearance of magnetic island chains at rational flux surfaces. Both trapped and passing particles can be rapidly transported across magnetic islands. Particle losses due to the magnetization of ferritic components can only be studied theoretically with complex numerical simulations where the full 3D structure

of the magnetic field is taken into account. The ASCOT code is one of the few tools in the world capable of such simulations and the results obtained during this thesis work will be further discussed in Sections 4.2.2 and 4.2.3 and in Publications IV and V.

The effect of TBMs on fast ion confinement was studied experimentally for the first time in dedicated experiments at the DIII-D tokamak in 2009 and 2012 [53]. In these experiments, the magnetic perturbation of the TBM was imitated by a set of coils in a TBM mock-up module installed in the first wall. Coordinated modelling efforts [54, 55], including the ASCOT simulations presented in Publication III, predicted localized fast ion losses caused by the TBM mock-up module. These results were confirmed by thermocouple and infra-red camera measurements taken at the tiles protecting the TBM mock-up module.

2.2.3 External coils

Virtually all of today's tokamak experiments are equipped with a set of coils for deliberately breaking the axisymmetry of the magnetic field with error fields. The breaking of axisymmetry can be used for mitigating instabilities, such as ELMs and Resistive Wall Modes (RWMs). On some tokamaks external coils are needed to correct error fields due to structural asymmetries. ELMs can be mitigated by perturbing the magnetic field near the edge of the plasma so that the heat and particle transport are increased in the pedestal, and the build-up and rapid collapse of steep pressure gradients is prevented. Since ELM mitigation is a critical issue in ITER [56], ITER design includes 27 coils built into the vessel in three rows of nine coils each, as illustrated in Figure 2.8. Experimental evidence suggests that ELM mitigation can be achieved with in-vessel coils without much of a loss in core performance [24]. The distribution of fast ions may be affected differently, however, since their wide orbits span a much wider range of flux surfaces.

Non-periodic magnetic perturbations generally create magnetic islands that degrade the magnetic confinement. A magnetic island creates a short-circuit by reconnecting magnetic field lines between regions that would normally be insulated from each other, allowing the plasma to flow freely between the two regions. If the islands become large enough to overlap, i.e., the Chirikov criterion [57] is fulfilled, the region covered by the islands becomes chaotic with all magnetic flux surfaces in the region ergodically connected to each other. Radial transport in such a region is

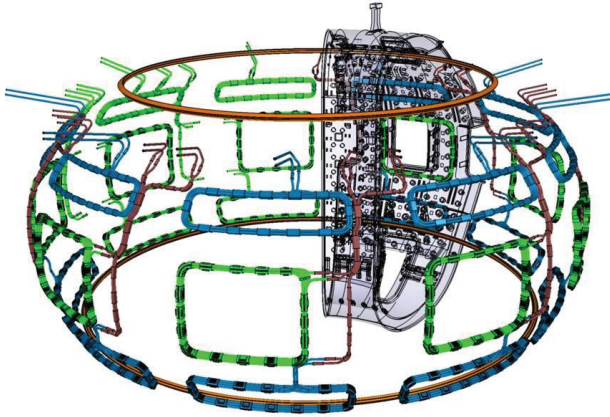


Figure 2.8. The in-vessel coils designed for ITER, arranged in three rows of nine coils inside the vacuum vessel on the outboard side. Each coil has its own power supply, which enables operation with different current waveforms. ©ITER organization

driven by the rapid transport parallel to the magnetic field which means particles can move almost freely across such ergodic regions. These effects are seen in vacuum modelling of the error fields generated by the ITER in-vessel coils. Figure 2.9 shows the results of a Biot-Savart calculation where the in-vessel coil current was scanned from 0 up to the maximum design value of 16 kA. An ergodic layer forms at the plasma edge and penetrates deeper into the core plasma as the coil current is increased.

The chaotic connection of magnetic field lines from the pedestal to the SOL and the formation of a 3D plasma boundary due to external coils has been observed in experiments at the MAST [58] and DIII-D [59] tokamaks. The application of resonant magnetic perturbations (RMPs) with high ($n > 3$) mode numbers was found to lead to a mitigation of ELMs, but also to an appearance of plasma “lobes”, or manifold structures, seen in visible light imaging near the X-point [60]. The formation of these lobes could be understood by numerical vacuum field-line tracing that predicted the ergodicity of the edge plasma. A pump-out of pedestal density is associated with the operation of ELM control coils in JET, MAST and DIII-D [24, 25, 58], and their effect on fast ions has been a field of active research in recent years. Since the orbits of fast ions are much wider than those of thermal plasma ions, fast ions born in the core plasma could be lost due to RMPs at the edge. Predictions for the impact of ELM coils on fast ion confinement in ITER have been carried out with the ASCOT code as an integral part of this thesis work and will be discussed in Section 4.2.3 and Publication V.

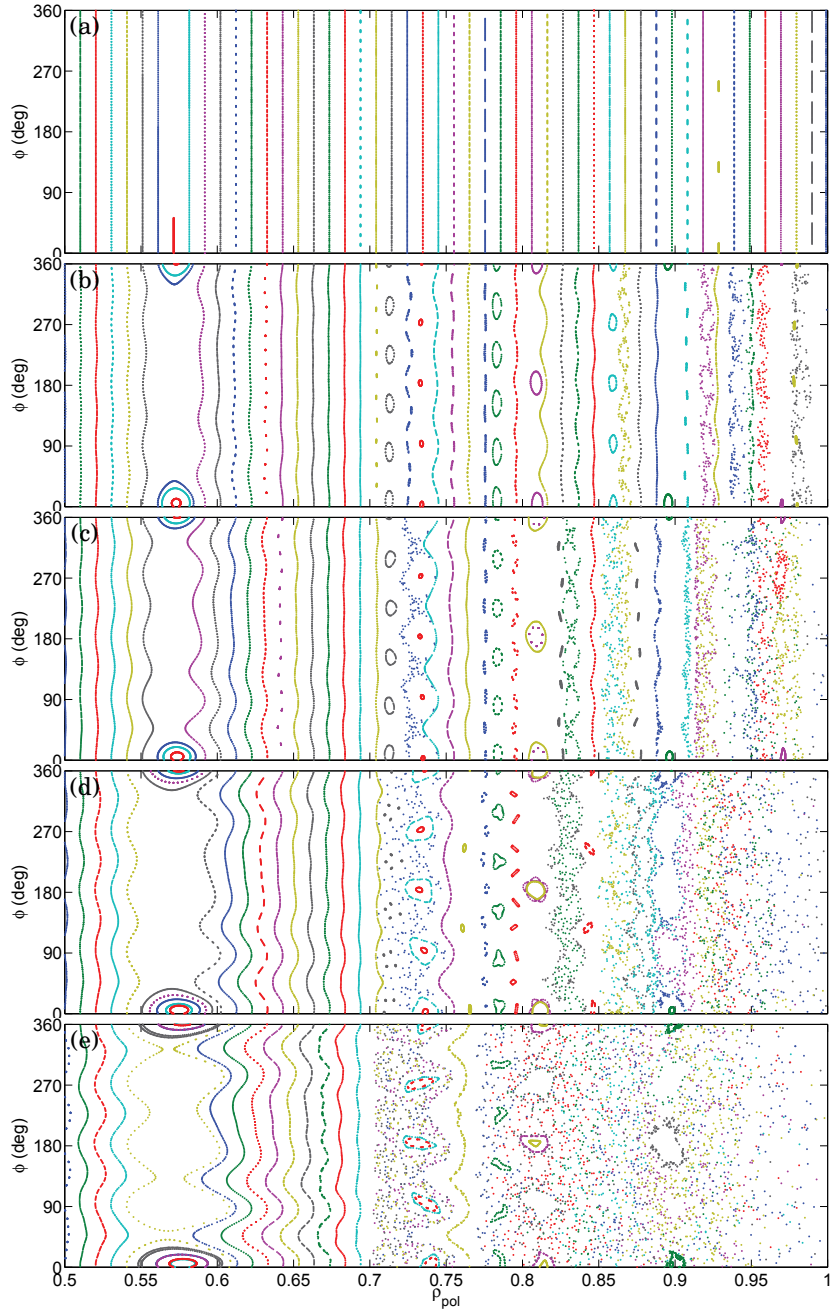


Figure 2.9. The onset of chaos in the magnetic field structure of ITER when external perturbations are applied. Poincaré plots from vacuum field tracing calculations by ASCOT show the in (ρ, ϕ) position of field lines intersecting the $\theta = 0$ plane. Islands and ergodic regions appear when the current in the in-vessel coils is increased from (a) 0 kA to 2 kA (b), 4 kA (c), 8 kA (d) and 16 kA (e), the maximum design value. Note that the coils have 6 turns, and the effective current is $16 \text{ kA} \cdot 6 \text{ turns} = 96 \text{ kAt}$. Different colors indicate field lines with different initial positions.

3. Tools and Methods

The tools and methods used in this thesis are simulation codes that solve the transport of particles in a tokamak. The main tool is the ASCOT code, used for fast ion modelling, which will be described in Section 3.1. ASCOT solves the kinetics of a trace ion species in a given background plasma with a Monte Carlo method. Because of the Monte Carlo approach, it can include realistic geometry and 3D effects that are often lacking in other models. Equilibrium of the background plasma for ASCOT is usually calculated by a transport code, such as JETTO [61], ASTRA [62] or TRANSP [63]. In Section 3.2 we shall briefly discuss the JET integrated transport modelling suite JINTRAC [64], which enables the self-consistent coupling of the 1.5D core transport code JETTO to ASCOT for simulating JET, MAST or ITER.

3.1 ASCOT

The ASCOT code is a Monte Carlo test particle orbit following code developed at Aalto University (formerly Helsinki University of Technology) and the VTT Technical Research Centre of Finland since the early 1990s. In ASCOT, the orbits of tracer test particles are followed in a static background plasma and the time-integrated distribution of the particles is solved. It is assumed that the population represented by the test particles is a trace minority, i.e. the background acts on the test particles but the test particles do not act on the background or on each other. The trace approximation is justified when the plasma is in steady-state, i.e., the heat deposited by the fast ions into the background plasma is compensated by heat transport and heat sinks. Since the trace particles do not interact with each other, the code parallelizes extremely efficiently.

The flow of data in ASCOT is illustrated in 3.1. The parts inside the light

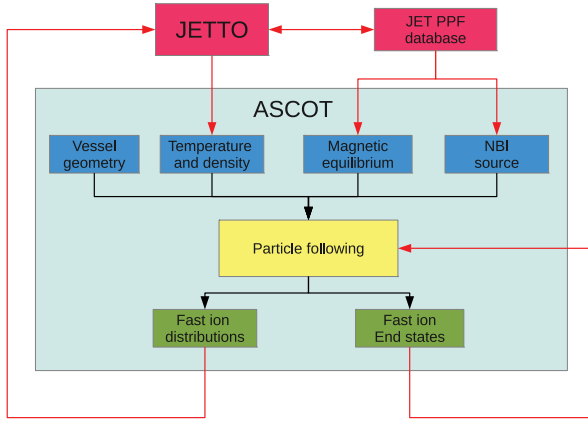


Figure 3.1. The flow chart of data in ASCOT (light blue box) and in JINTRAC (red loop). The light blue box contains the stand-alone, once-through process of ASCOT, which reads input data, processes the test particles, and writes output. When coupled to a transport code, such as JETTO, the process is repeated iteratively.

blue box are the stand-alone ASCOT that is a batch process that reads input data, processes it, and produces output. In stand-alone ASCOT, steady-state plasma conditions and external fast ion sources are supplied by the user. Test particles are sampled from a constant fast ion source and followed until thermalized or lost to the vessel wall. Data is gathered during particle tracing into distributions of physical quantities, such as density, torque and heat flux. When particles are lost to the wall, their end states are stored. At the end of the simulation, the distributions describe the steady-state slowing-down distribution of the simulated fast ions and the end states describe the power flux of lost fast ions to the wall.

A coupling with a transport code, such as JETTO, has been added around the stand-alone ASCOT as indicated by the red loops in Figure 3.1, to give the model a degree of self-consistency. The JETTO-ASCOT coupling is discussed in Section 3.2.1.

3.1.1 Brief history of ASCOT

At the time of writing of this thesis, two versions of ASCOT are available and, consequently, have been used in the studies presented in this thesis. Since ASCOT has been in constant use and development since the 1990s, a need for a complete re-write was recognized, and the work on

a new version, ASCOT4 [29], was started in 2010. ASCOT4 comprises all the physics models as the previous versions of the code, but has been rewritten using modern programming conventions to consist of independent modules that can be used for various analysis tools. In fact ASCOT4 is not a code, but a suite of codes using a set of common physics modules. The codes that make use of the modules in ASCOT4 include FILIP: a field line Poincare surface tracing tool, BioSaw: a Biot-Savart law solver and AFSI: a fusion reaction source integrator. The development of new physics models is planned exclusively for ASCOT4.

Although version numbers of ASCOT have not been previously used, the new version was labelled “4” to reflect the previous development stages. The first version of ASCOT, described in [65] can be referred to as “ASCOT1”. “ASCOT2” was developed in the late 90s and included tabulated numerical background data instead of analytic models [66] and parallelization via MPI. The code developed in the 2000s, best described in Ref [67], and used in Publications IV, III, II and I of this thesis is to be called “ASCOT3”. ASCOT3 introduced a 3D tabulated magnetic field module and the possibility of full-orbit (FO) following. ASCOT4 has only recently entered production use, the first results have been published in Publication V and [68] and a detailed description of ASCOT4 is given in Ref [29]. In this thesis, references to ASCOT without a version number refer to the common physics models found in both versions 3 and 4. References to ASCOT3 or ASCOT4 refer to the specific versions of the code. Furthermore, a hybrid version, ASCOT3.5, exists and is in sporadic use. It incorporates the magnetic field module of ASCOT4, but uses the basic structure of ASCOT3. ASCOT3.5 has not been used in the work presented in this thesis.

3.1.2 Background data

In order to run a simulation, ASCOT needs information about the plasma facing surface of the vessel, the temperature and density of the plasma, the magnetic equilibrium and external fast ion sources. By default, the background data are assumed static in ASCOT and the simulations always describe a steady-state. This restriction is partially lifted in the dynamic JETTO-ASCOT coupling in JINTRAC, which will be discussed in Section 3.2.1, but for now the background is assumed static. Background data is given on a discrete, uniform grid that can be arbitrarily chosen to cover the simulation domain. Most background data can be provided on a 1D, 2D or 3D grid. Since ASCOT is not solving the electric and magnetic

fields, the structure of the grid does not play a large role in the results of the code. ASCOT only needs to interpolate the data on the grid, with derivatives continuous to second order.

Information about the first wall structure is needed to determine orbit losses and calculate fast ion wall loads. The vessel wall data consists of the outermost plasma-facing limiter surface as a 2D contour in R, z , assumed independent of the toroidal location, or a 3D model of the whole plasma facing surface as a list of 3D polygons. The 3D model for the vessel wall can be generated by defeating CAD data to a desired level of accuracy. This has been done in material migration studies for JET and ASDEX Upgrade [69, 70]. Much more simplified 3D models have been used to highlight the 3D structure of, e.g., limiters, in ITER studies such as Publication IV and Ref. [71].

The magnetic equilibrium consists of a 2D map of the equilibrium poloidal flux $\psi(R, z)$ and the poloidal current function $f'(\psi)$. These quantities are obtained by solving the Grad-Shafranov Equation [4]. The Grad-Shafranov equation is typically solved by an iterative numerical algorithm in codes such as EFIT [72] and the solution is obtained on a (R, z) grid that encompasses the whole poloidal cross-section of the vacuum chamber. A cylindrical coordinate system is used in ASCOT for advancing the equations of motion and, therefore, contrary to codes using a straight field line coordinate system, both open and closed field line regions can be simulated. The poloidal flux is related to the poloidal magnetic field by

$$B_R(R, z) = \frac{1}{R} \frac{\partial \psi(R, z)}{\partial z} \quad (3.1)$$

$$B_z(R, z) = -\frac{1}{R} \frac{\partial \psi(R, z)}{\partial R} \quad (3.2)$$

and $f'(\psi)$ is related to the toroidal field by

$$f'(\psi) = RB_t. \quad (3.3)$$

The magnetic field of a tokamak typically has two special points where $\nabla\psi = 0$, the X-point and the magnetic axis. In these special points the equilibrium magnetic field is determined by equation (3.3) alone and the field lines are purely toroidal. Due to the ∇B drifts, however, particles will quickly drift out of these points and they do not need any special treatment in ASCOT.

Instead of ψ , the square root of the normalized poloidal flux

$$\rho = \sqrt{(\psi - \psi_{ax})/(\psi_{sep} - \psi_{ax})}, \quad (3.4)$$

where ψ_{ax} and ψ_{sep} are the poloidal fluxes at the magnetic axis and the magnetic separatrix, respectively, is used as the flux surface label in ASCOT and throughout this thesis. The magnetic field can include 3D perturbation components which are given as cylindrical components of the magnetic field $B_R(R, \phi, z)$, $B_z(R, \phi, z)$ and $B_t(R, \phi, z)$. Details of the magnetic field format are documented in [67]. Harmonic perturbations, such as the TF ripple, can also be included by defining $\delta(R, z)$ and N_c from Equation (2.10) and calculating the components of \mathbf{B} on the fly. Such a harmonic ripple model is implemented in ASCOT and described in [73, 74]

The background plasma temperature and density data required by ASCOT are typically obtained from a transport code, or directly from measurements. In the plasma core, temperature and density can be assumed constant on flux surfaces and it is therefore sufficient to supply them as radial 1D profiles that can be mapped to the flux surface label ρ . In the SOL, and in cases where there is significant poloidal transport in the core, 2D maps in (R, z) can be used by ASCOT.

3.1.3 Fast ion sources

Models for the sources of NBI ions and fusion products are fully integrated into ASCOT. The proper treatment of the source of ICRH ions requires a self-consistent treatment of the interplay of the wave field and the fast ion distribution. Work for integrating the RFOF library [75] for calculating the ICRH source is underway. At the moment, a simplified, ad-hoc, ICRH source exists [29].

The source of NBI ions is calculated with the BBNBI module [76], integrated into ASCOT. The BBNBI module contains the detailed geometry of the NBI injectors and models the beam as a set of individual beamlets from which test particles are picked with a Monte Carlo algorithm. The location, direction and divergence of each beamlet can be specified individually, and the fractions of the W_0 , $W_0/2$ and $W_0/3$ energy components are taken into account for each injector. At the time of writing this thesis, the NBI geometries of JET, ITER, ASDEX Upgrade, DIII-D, FAST, TEXTOR, MAST, and Tore Supra have been implemented.

For a source of fusion products, the fusion reaction rate distribution is first calculated by the AFSI module in ASCOT4. The thermal fusion reaction rates are calculated using cross-sections parametrized as functions of density and temperature [77]. Beam-target and beam-beam fusion reaction rates are calculated from the distribution of fast ions in velocity

space, obtained from a beam ion simulation, by calculating the integral

$$\mathcal{R} = \int \sigma \mathbf{v} n_i n_j d\mathbf{v}^3, \quad (3.5)$$

where σ is the atomic cross-section of the fusion reaction, \mathbf{v} is the centre-of-mass velocity and n_i and n_j are the density distributions of the reacting particles. The fast ion distribution function reacts with a Maxwellian distribution in beam-target reactions and with itself in beam-beam reactions.

Test particles are sampled from \mathcal{R} with either a weighing scheme or uniform weights. In the weighing scheme, the test particles are distributed uniformly in space and the distribution of real particles is represented by assigning a weight factor to each test particle. Weighing is useful for obtaining good statistics in studies dependent on only a small fraction of the fast ion population, e.g., fusion product losses. The weights are calculated as

$$w_i = \int_0^{2\pi} \mathcal{R}(\rho_i) R_i d\phi \frac{\int_0^1 \mathcal{R}(\rho) V(\rho) d\rho}{\sum_{i=1}^N \int_0^{2\pi} \mathcal{R}(\rho_i) R_i d\phi}, \quad (3.6)$$

where w_i is the weight of the i :th particle, $\mathcal{R}(\rho)$ is the fusion reaction rate with $\mathcal{R}(\rho_i)$ being the reaction rate evaluated at the location of the i :th particle, R is the major radius and $\int_0^{2\pi} R d\phi$ is the volume ratio of any two axisymmetric volume elements with an equal poloidal cross-section, N is the total number of particles, $V(\rho)$ is the flux surface volume, ρ is the square root of the normalized poloidal flux, and ϕ is the toroidal angle. In the uniform weight scheme, the weights of all test particles are equal and the test particle distribution is representative of the distribution of the real particles. This produces the best statistics for the distribution as a whole. Particles are generated by rejection sampling against $\mathcal{R}(R, \phi, z)$, where the coordinates R , ϕ and z are sampled from a probability distribution uniformly distributed in volume. The weight factors for all particles are now equal, calculated simply as

$$w_i = \frac{\int_0^1 \mathcal{R}(\rho_p) V(\rho) d\rho_p}{N}. \quad (3.7)$$

In both schemes, the weight factors have the dimension s^{-1} , i.e. the test particles represent a steady-state particle source. The initial velocities of the particles are chosen so that the velocity distribution is isotropic. The birth energy of fusion products has been assumed to be a delta function in the studies reported in this thesis. However, this assumption can be refined in ASCOT4 by taking into account the thermal energy distribution of the reacting particles [78].

3.1.4 Monte Carlo orbit following

The orbits of the test particles are followed in ASCOT from their birth position, typically until they reach thermal energy or hit the vessel wall. In most situations the Guiding Center (GC) approximation is valid and the motion of the guiding center described by Equation (2.7) is advanced with a fourth order Cash-Karp Runge-Kutta algorithm [66] in cylindrical coordinates. When necessary, the full gyro-orbit (FO) of the particle, Equation (2.1), can be integrated with a second order leap-frog Boris algorithm [79], which typically increases the computational time by an order of magnitude.

Pitch angle scattering and slowing-down by Coulomb collisions with a Maxwellian background are evaluated with Monte Carlo operators, based on the work of Boozer and Kuo-Petravic [80]. The implementation of the collision operator in ASCOT4 has been published in recent theoretical works by Hirvijoki et.al. [29, 38, 81] and, therefore, the details are omitted here. The operator consists of a deterministic friction term and a stochastic diffusion term and drives the test particle towards the background Maxwellian distribution. In the GC picture, the operator acts on energy and pitch of the guiding center and has the following form

$$\Delta E = \left(-\nu v + \frac{\partial D_{\parallel}}{\partial v} + 2 \frac{D_{\parallel}}{v} \right) \Delta t \pm \sqrt{2 D_{\parallel} \Delta t} \quad (3.8)$$

$$\Delta \xi = -\xi \frac{2 D_{\perp}}{v^2} \Delta t \pm \sqrt{(1 - \xi^2) \frac{2 D_{\perp}}{v^2} \Delta t}, \quad (3.9)$$

where \pm indicates an uniformly distributed random sign. In the FO picture the velocity vector of the test particle is deflected by a small angle α , determined by $\cos \alpha = 1 - 2 D_{\perp} v^{-2} \Delta t$, in a random direction, and the speed is scaled to change the energy of the particle by ΔE from Equation (3.8). The scalar coefficients D_{\parallel} , D_{\perp} and ν used in the operator are functions of the velocity of the test particle, the temperature and density of the background plasma and their respective mass and charge numbers. The derivation of the coefficients can be found, e.g., in [29] and references therein.

The interaction timescales of the test ions can be accelerated to achieve faster simulations without loss of accuracy [66]. Fast ions are typically almost collisionless and will complete a large number of orbits per collision mean free path. In an axisymmetric magnetic field, collisionless orbits close upon themselves and simulating several collisionless orbits with the same initial conditions yields no additional information. In ASCOT,

the cumulative background interactions over several orbits can be applied during a single orbit when simulating particles in an axisymmetric field. However, in a non-axisymmetric magnetic field the acceleration is, generally speaking, not applicable since collisionless orbits can evolve due to 3D effects. A good example of this is the stochastic ripple diffusion that was discussed in Section 2.2.1. In the results presented in this thesis, timescale acceleration has only been used in Publications I and II that focus on validation in cases where 3D effects are not important. In Publications III, IV and V, the acceleration has not been used and the full slowing-down history of the particles has been simulated.

Models for other interactions can be activated when specific phenomena are being modelled. These interactions include anomalous diffusion due to microturbulence [71], MHD modes [68], scrape-off layer flows [69] and atomic reactions [69].

Collisions of test particles with the vessel wall are recorded with a ray-tracing algorithm [82] to resolve the exact positions of wall hits. An algorithm for switching from GC to FO following in the vicinity of the wall has been implemented to increase the precision of wall hits with little extra computational cost [79].

3.1.5 Numerical diagnostics

There are two standard types of outputs in ASCOT: distributions and test particle end states. Distributions contain the time-integrated history of the simulated trajectories of the particles, i.e. the moments of the Monte Carlo solution to the kinetic equation of the fast ions. Test particle end states contain the data of fast ion loss and thermalization rates. In coupled simulations, the end state data are also used to initialize the next simulation step.

The distributions are stored in N-D histograms, where the N abscissae correspond to phase-space coordinates. For compatibility with 1D transport codes, most distributions are gathered as flux-surface averaged radial profiles as a function of ρ . Any distribution can also be output as a 2D R, z profile and, in addition, the density distribution can be output as a 4D $R, z, v_{\parallel}, v_{\perp}$ or R, z, ξ, W profile. Signals of synthetic diagnostics, such as a neutral particle analyser or a neutron detector can be calculated by integrating the 4D distribution. This will be revisited in Section 3.4.

To record fast ion distributions, the contribution of the test particle is added to the histograms, in the bins passed through during the orbit fol-

lowing time step Δt . If the test particle moves through more than one bin during Δt , linear interpolation is used to distribute the weight among the bins, simultaneously in all abscissae the histogram. The contribution is obtained by multiplying the weight of the particle by the physical quantities of interest. The following 1D and 2D profiles are the main physics outputs of ASCOT: particle density (3.10), energy density (3.11), current density (3.12) collisional power deposition to the plasma (3.13), toroidal $\mathbf{J} \times \mathbf{B}$ torque (3.14), toroidal collisional torque (3.15), toroidal torque from changes in toroidal canonical momentum P_ϕ (3.16), fast ion pressure (3.17) and beam-target fusion rate (3.5). The corresponding contributions are [29]

$$w_n = w\Delta t \quad (3.10)$$

$$w_W = Ww\Delta t \quad (3.11)$$

$$w_j = evw\Delta t \quad (3.12)$$

$$w_{P,c} = -\Delta Ww \quad (3.13)$$

$$w_{\tau,jxB} = -e\Delta\psi_p w \quad (3.14)$$

$$w_{\tau,c} = -R \left(\Delta p_\parallel \frac{B_T}{|B|} \right) w\Delta t \quad (3.15)$$

$$w_{\tau,p_\phi} = -e\Delta P_\phi w \quad (3.16)$$

$$w_p = mv^2 w\Delta t. \quad (3.17)$$

Here w is the test particle weight factor indicating how many real particles it represents, W the kinetic energy, e is the unit charge, v is the velocity, B_T is the toroidal magnetic field, B is the total magnetic field, $\Delta\psi_p$ and ΔP_ϕ the changes in particle position and canonical toroidal momentum due to the orbit integration, and ΔW and Δp_\parallel are the changes in energy and parallel momentum due to the collisional friction with the background in Δt . In addition, for coupled transport simulations, the thermal ion and neutral particle, energy and momentum sources and sinks are calculated by tallying up the weights of thermalized and neutralized test particles and using equations (3.10), (3.11) and $w_{\tau,th} = mv_\phi R w\Delta t$, respectively.

Fast particle wall power loads are calculated from the end states of lost particles, which contain relevant parameters of the lost particle, such as mass, charge, location, velocity and energy. Each lost test particle constitutes a power flux at a point on the vessel wall in steady-state conditions. This data can be gathered in post-processing to obtain a map of total fast ion loss power flux to the first wall. Over the course of this the-

sis work, postprocessing routines in MATLAB were developed to visualize the wall load maps produced by ASCOT3, and later ported to ASCOT4. The wall load data produced by ASCOT is natively in 3D, but it can be mapped to a 2D (ϕ, θ) grid, or averaged to a 1D grid of either ϕ or θ . These plotting tools have been used in recent publications by the ASCOT group [28, 71, 79, 83, 84] and in the studies presented in Chapter 4 of this thesis. An example of mapping of the lost alpha particle power load in the ITER 15 MA standard operating scenario is shown in Figure 3.2. The 2D mapping assumes radial line segments out from the magnetic axis only intersect the first wall surface once. In the tips of the divertor legs and on purely radial wall segments this condition is violated and the data is incorrectly represented. To explore the the wall load in full detail, a 3D representation has to be used [69–71]. The 2D mapping is useful since it is equivalent for all machines and the regions of interest for fast ion losses are typically below the outer midplane on the outboard side of the machine, where the mapping to (ϕ, θ) works very well.

The calculation of power flux density per surface area (W/m^2) is nontrivial due to the test particle tracing method used in ASCOT. Since the power flux density is represented by a finite number of point-like test particles, spread over a finite surface area, it has to be ensured that each area element is large enough to have sufficient test particle statistics, while small enough to produce a sufficient resolution on the plasma facing surface. Since variations of several orders of magnitude are often found in the simulated fast ion wall load (from kW/m^2 to MW/m^2), it should be kept in mind that the statistics is often poor in areas where the magnitude of the power load is low. However, wall load studies typically look for the hot spots on the wall, which usually have good test particle statistics. Another cause for statistical error arises from the particle weighing scheme. The weighing scheme in Equation (3.6) has been used in ITER wall load studies of fusion products in this thesis, since it allows the loading of the majority of the test particles close to the edge where they are more likely to be lost and, therefore, the statistics of losses are improved. However, in ITER plasmas, the fusion reaction rate \mathcal{R} often varies by several orders of magnitude between the core and the edge. Therefore, lost particles from deep in the core can represent large, but statistically inaccurate heat load spikes on the wall. Variance reduction techniques [85] could be employed in the future to improve the resolution and statistics of the wall loads calculated by ASCOT. Statistical confidence intervals could be calculated by

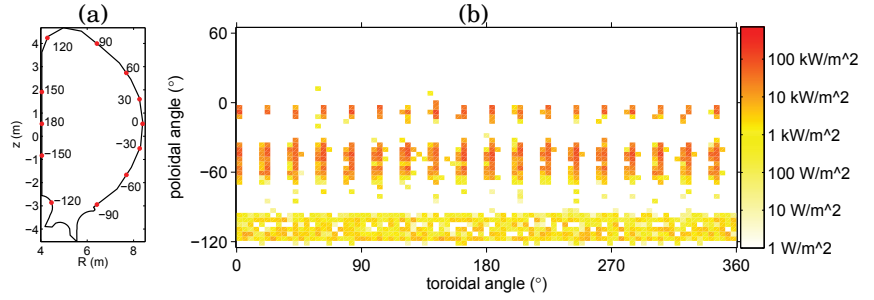


Figure 3.2. The 2D contour of the ITER first wall and the definition of the poloidal angle used in the mapping of fast ion losses (a). The mapped wall load due to lost alpha particles in the ITER 15 MA standard operating scenario using a first wall model with 18 continuous poloidal limiters (b).

resampling the test particle data in a procedure known as bootstrapping. These methods are outside the scope of this thesis, but worth considering for future work. In the ITER wall load studies presented in this thesis, such as the example shown in Figure 3.2, a physics-based approach has been taken to the resolution of the wall loads: Since the heat deposited by the particle is conducted into the wall material, the power flux has been calculated on $4^\circ \times 2^\circ$ area elements that roughly correspond in size to the 150 cm^2 solid metal blocks, so-called “fingers”, that form the first wall thermal shield in ITER [86]. The losses test particles with unreasonably large weight factors was monitored, but they did not have a significant effect on the results.

3.2 JINTRAC

The JET Integrated modeling suite JINTRAC [64] is a suite of codes that solves the transport of particles, heat and momentum self-consistently in a coupled core-edge system. It consists of magnetic equilibrium solvers (EFIT, CREATE-NL, ESCO), a 1.5D core transport solver (JETTO-SANCO), a 2D edge transport solver (EDGE2D-EIRENE), auxiliary heating solvers (ASCOT, PENCIL, PION) and many other auxiliary physics models. References to the individual codes within JINTRAC may be found in Ref. [64]. At the time of writing of this thesis, JINTRAC can only be executed in serial, on the JET Analysis Cluster (JAC) because of its dependence on JET internal libraries. Due to increasing demands for computing power, work is underway to port and parallelize JINTRAC to supercomputing platforms available in Europe and worldwide.

Transport codes typically solve numerically the equations for the evolution of the first three velocity moments, i.e., particles, momentum and heat, corresponding to the distribution function and close the system of equations with a transport model. Transport models relate the fluxes of particles, heat and momentum to lower-order quantities of the system, such as density, temperature and their gradients. Different core transport models are available in JINTRAC: neoclassical transport model NCLASS, semi-empirical anomalous transport Bohm-gyro-Bohm model, and drift wave models such as Weiland, GLF23 and TGLF. The power of JINTRAC is in interfacing of codes dealing with different domains. The core and edge transport codes pass boundary conditions from one to the other, removing the need for artificial user-set boundary conditions. By solving the core and the edge simultaneously the boundary of the integrated system is moved to the far SOL and the divertor targets. On top of the coupled transport model, codes calculating the sources of density, particles and momentum are coupled to the suite. In this context, ASCOT provides the self-consistent calculation for the NBI heating source.

3.2.1 ASCOT in JINTRAC

ASCOT is available in JINTRAC as a NBI heating module, an alternative to the 1D Fokker-Planck code PENCIL [87]. The main advantages of ASCOT are the full 3D kinetic treatment of fast neutral and ion dynamics and the inclusion of realistic geometry, but it comes at a cost of an order-of-magnitude increase in computation time. In a JINTRAC simulation, as indicated by the red links in Figure 3.1, ASCOT periodically communicates with the core transport solver JETTO, which provides the kinetic core plasma profiles. The particle, heat and momentum source distributions calculated by ASCOT are used by JETTO to calculate the new kinetic core profiles that are fed back into ASCOT in the next communication step. The communication intervals between ASCOT and JETTO are kept much shorter than the NBI slowing-down time, typically of the order of 10 ms, and the loop continues until the plasma has been evolved for a pre-set time. In this scheme, ASCOT becomes part of a time-dependent simulation where the background plasma can not assumed to be in steady state throughout the slowing-down time of the NBI ions. This requires a slightly different interpretation of the test particles. They are no longer sampled from a steady-state particle source but rather, to keep heating the plasma, new NBI ions must be continuously added into the simula-

tion while keeping the number of test particles in the simulation approximately constant for numerical stability. New test particles are therefore added at a rate which corresponds to the sink of NBI ions due to ionization and orbit losses, and their weight factors are dimensionless. The coupled simulation typically runs for a large number of NBI slowing-down times. The output distributions produced by ASCOT also have a slightly different interpretation in JINTRAC simulations. Rather than describing a steady-state slowing-down distribution, they are time-slices of the time-dependent slowing-down distribution as it evolves in time. The JINTRAC-ASCOT coupling has been successfully exploited for predictive studies of ripple experiments [44], current drive studies [88], momentum transport studies [89] and the work reported in Publication I.

Until very recently, JETTO has been a serial program and in order to take advantage of the parallelization of ASCOT, ASCOT has been executed as a separate executable. During an integrated simulation, both ASCOT and JETTO are running simultaneously, one waiting idle while the other is processing. The communication is done via files on the filesystem. Recent JETTO development is moving towards parallelizing the whole code to take advantage of more sophisticated transport models, such as the TGLF gyro-fluid model, which require executing in parallel. Further down this development path, ASCOT4 will be integrated into the parallel main program as a subroutine.

3.3 Tokamaks of interest

This thesis work includes simulations performed on several existing tokamaks, as well as predictive simulations for ITER that is still under planning and construction. Each of the existing tokamaks studied, DIII-D, JET and TEXTOR, have some unique features that warranted their study. In this section, the tokamaks that have been studied in this thesis are briefly described. The main operational parameters of each tokamak are summarized in table 3.1.

The Joint European Torus (JET) [90] in Culham, UK, is the largest operating tokamak in the world and the flagship of the European fusion program. In 2011, JET was refurbished with a beryllium first wall and a tungsten divertor [91], an identical material mix to the one to be used in ITER. Therefore understanding the behaviour of JET plasmas with the ITER-Like Wall (ILW) is of utmost importance for preparing for ITER op-

eration. JET currently holds the world record for highest fusion energy production, and is set to surpass that record in 2017 when another DT experiment campaign is planned. After the DT campaign, JET is scheduled to shut down.

The DIII-D tokamak [92] in San Diego, USA, is the largest magnetic confinement experiment in the USA. It is a medium-sized divertor machine with a total of four co- and counter-current neutral beams and a large array of diagnostics. In 2009 and 2011 DIII-D performed unique experiments where the axisymmetric magnetic field was locally perturbed with a set of coils, simulating the effect of the TBMs in ITER. These TBM mock-up experiments presented a unique opportunity to study local fast ion losses by measurements and modelling.

The Tokamak Experiment for Technology Oriented Research (TEXTOR) [93] was in operation in Jülich, Germany, until 2013. It was a circular cross-section limiter tokamak with two neutral beam boxes. TEXTOR was mostly used for experiments in materials research, but it was also equipped with a collective Thomson scattering diagnostic [94] that made it possible to directly measure parts of the fast ion velocity distribution.

The ITER tokamak [95] (previously International Thermonuclear Experimental Reactor, nowadays latin for “the way”), is under construction in Cadarache, France, and is expected to begin operation in the 2020s. The aim of ITER is to demonstrate the technical feasibility of fusion energy production. For that purpose, it will aim to operate a DT plasma at a fusion gain of $Q = 10$ in ELMy H-mode. ITER will have a relatively low number of superconducting toroidal field coils compared to its size, local ferritic tritium breeding modules embedded in the first wall, and resonant magnetic perturbations for ELM control. The neutron irradiation environment in ITER puts stringent restrictions on the diagnostics that can be operated, and access to the machine is done entirely via remote handling. The fate of fast ion diagnostics in ITER is still uncertain, all the more reason to develop our understanding of the fast ion physics via modelling.

3.4 Measuring the fast ion distribution

Measuring the 6D (r, v) distribution of fast ions in a tokamak is extremely difficult, which is why fast ion modelling is crucial for understanding the behaviour of fast ions in the plasma. Diagnostics able to measure small

Table 3.1. Main parameters for the tokamaks simulated in this thesis. Note that the parameters for ITER are predictions.

Name	JET	DIII-D	TEXTOR	ITER
In operation	1983 - 2019?	1986 -	1981 - 2013	202* -
Location	Culham, UK	San Diego, USA	Jülich, Germany	Cadarache, France
Configuration	Divertor	Divertor	Limiter	Divertor
Major radius	2.96 m	1.66 m	1.75 m	6.2 m
Minor radius	0.9 m	0.67 m	0.47 m	2.0 m
Plasma volume	100 m ³	24 m ³	7 m ³	700 m ³
Heating power	41 MW	31 MW	9 MW	73 MW
Maximum B_t	4.0 T	2.2 T	2.8 T	5.3 T
Maximum I_p	6.0 MA	3.0 MA	0.8 MA	15.0 MA
Typical pulse length	10 s	5 s	10 s	1000 s
Ripple amplitude	0.08 %	0.5 %	1.5 %	1.1 % ¹
Wall material	W+Be	C	C	W+Be

¹ Ripple amplitude in ITER is 1.1 % when uncompensated by ferritic inserts.

With the designed ferritic compensation, it is between 0.2 % and 0.5 %.

parts of the fast ion distribution exist, but they are typically localized in phase-space or integrated over most of the dimensions of the distribution. As an example, Figure 3.3 illustrates the coverage of fast ion diagnostics in JET and MAST. The purpose of this section is to give a brief overview on fast ion diagnostics available at different tokamaks worldwide and give examples of how to compare fast ion simulations and diagnostics. Fast ions can only be “directly” measured when they are lost from the plasma, but only a narrow slice of the distribution is lost. The measurements of the confined fast ion distribution mostly rely on diagnosing the spectra of waves and particles emitted from atomic reactions in the plasma involving the fast ions. Most commonly used signals are fusion neutrons, charge exchange losses, MeV gamma-rays and Balmer D_α lines.

The most straightforward way is to measure the fusion neutrons. In today’s experiments, the fusion reaction rate between thermal plasma ions is very low due to the relatively low temperature and the reluctance to use tritium due to radiation safety. In NBI or ICRH heated plasmas, reactions between fast and thermal deuterium or tritium dominate, and the produced neutrons (recall Equations (1.2) and (1.3)) are promptly lost. The measured neutron flux is a good proxy for the fast ion density, inte-

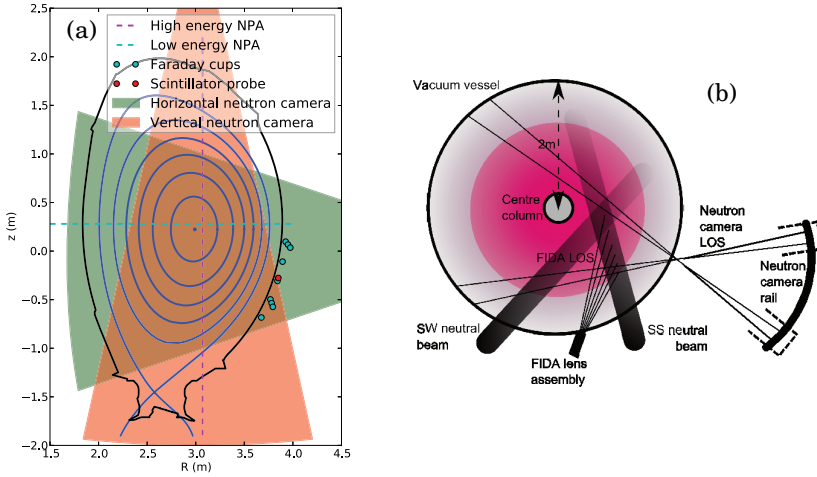


Figure 3.3. The coverage of fast ion diagnostics on (a) JET and (b) MAST. JET is equipped with both horizontally and vertically viewing neutron cameras that can be used to reconstruct the fast ion density in (R, z) in the plasma core. MAST is equipped with a FIDA diagnostic that gives a localized measurement along the path of the neutral beam, as well as a rotating neutron camera that can be moved to obtain a (line integrated) profile over several shots.

grated over the velocity space, along the line of sight of the detector. An array of line of sight measurements can be inverted to evaluate the fast ion density profile [96], and the fast ion temperature can be inferred from the broadening of the neutron energy spectrum [97]. A synthetic neutron diagnostic is routinely produced by codes such as ASCOT. The fusion reaction rate profiles can be calculated as an integral over the simulated fast ion distribution function, as was discussed in Section 3.1.3, and synthetic neutron diagnostic signals can be calculated by line integrating the reaction rate profile.

Some nuclear reactions, fusion and otherwise, produce MeV gamma-rays with distinguishable peaks in the energy spectrum. Reactions have been identified for fast H,D,T and α particles with various energy thresholds [98]. The gamma-ray spectrum can, therefore, be used to evaluate the density of confined fast ions above the threshold energy of a given reaction. Analogous to neutron spectroscopy, the Doppler broadening of the gamma peaks can be used to estimate the average temperature of the fast ions. Simulating the gamma-ray spectrum requires detailed atomic data and some dedicated codes for this exist, e.g., the GAMMOD code [98].

Charge exchange reactions between fast ions and neutrals in the plasma

produce fast neutrals that are promptly lost. These neutrals carry a footprint of the confined fast ions and can be measured with the Neutral Particle Analyzer (NPA) [99]. In the NPA, the lost atoms are first re-ionized and then spatially separated in energy and mass/charge ratio by electric and magnetic fields. Finally, the ions are counted by an array of ion detectors. NPA signals can in principle be easily extracted from fast ion simulations. If the fast ion distribution and neutral particle distributions are known, atomic cross-section data can be used to calculate the rate of CX reactions along the line-of-sight of the detector. The atomic data is fairly well known and catalogued in databases such as ADAS [100], but neutral particles in the core are often poorly diagnosed which creates large uncertainties in synthetic NPA diagnostics [101–103].

Fast ions that undergo charge exchange with injected neutral beam particles emit Balmer D_α light with a large Doppler shift that can be used to separate it from D_α light from the bulk plasma. The fast ion D_α (FIDA) line is typically emitted before the fast ion moves more than a few centimetres and, therefore, gives fairly accurate information on the spatial fast ion distribution [104–106]. Synthetic FIDA signals can be computed by, e.g., the FIDASIM code [107] using a fast ion distribution simulated by codes such as ASCOT. Recently, tomographic inversion techniques have been developed and applied for reconstructing the local velocity space distribution of fast ions [108] from FIDA signals, which can be directly compared to fast ion simulations.

A different approach is to actively probe the fast ion distribution. The Collective Thomson scattering diagnostic (CTS) measures the spectrum of the millimetre-wave radiation reflected from a probe beam scattered off collective fluctuations due to the motion of ions in the plasma. The scattered spectrum carries information about the distribution of the ion velocity distribution projected along the fluctuation wave vector. The CTS therefore allows measuring the 1D projection of the ion distribution function in velocity space, locally in real space [94, 109]. The projection of the fast ion distribution can be inferred from the high-energy tails of the measured distribution. The measured 1D projection of the fast ion distribution can be calculated from a simulated fast ion distribution, which has been demonstrated in, e.g. [110] and Publication II. At ASDEX Upgrade, the CTS and FIDA diagnostics have recently been combined for accurate fast ion velocity space tomography [111].

Lost fast ions can be diagnosed locally by diagnostics such as Faraday

cups [112] and scintillator probes [113]. Scintillator probes resolve the lost fast ions in terms of their pitch and energy based on their impact positions on a detector plate, viewed by a fast camera. Faraday cups resolve the energy of lost ions by their penetration through a stack of thin foils but do not offer pitch resolution. Since lost fast ions tend to originate from a very narrow region in phase space, fast ion loss diagnostics only provide information about changes in the confinement of fast ions, not the distribution itself. Fast ion simulation codes whose computational domain includes the open flux surfaces and the vessel wall, such as ASCOT, routinely produce the lost fast ion flux (see e.g., Ref [83] for ASCOT modelling of FILD signals), as was discussed in Section 3.1.5.

4. Results

The main goal of this thesis work is to provide reliable predictions of fast ion losses for ITER. This has been achieved by developing the ASCOT code to be one of the most sophisticated codes in the world for fast ion simulations, and applying it to ITER operating scenarios. To ensure the validity of the code, a number of studies on existing machines were carried out with the intent of benchmarking the results from ASCOT to experimental data and to other established codes in the field. Publications I, II and III describe studies where data extracted from ASCOT simulations were compared to measurements and simulations made in experiments performed on JET, TEXTOR and DIII-D, respectively. These results are summarised in Section 4.1. Publications IV and V describe predictive ASCOT simulations for two ITER operating scenarios in which the losses of fast ions and the associated wall power loads were calculated. These results are summarised in Section 4.2.

4.1 Fast ion studies on existing tokamaks

It should be noted that this thesis is not the first effort to validate ASCOT (see e.g. Refs [74, 101, 114]). However, as new features are developed in the code and new diagnostics become available, new benchmarks should be made. In particular, the 3D magnetic field model in ASCOT was developed for ITER simulations described in Publication IV, and had not been used on any existing tokamak before the studies reported in Publication III and in [54].

4.1.1 Modelling the effect of the JET ITER-like wall on neutral beam deposition

After the installation of a metallic ITER-like wall (ILW) at JET in 2011 [91] a low pedestal temperature and a peaked profile shape have been observed, leading to poor plasma performance compared to experiments with the previous, carbon, wall. Due to the metallic wall, the mix of impurities in the plasma changed from predominantly carbon to beryllium and tungsten, the same impurities that will be present in ITER plasmas. Therefore, the effect of these impurities on the core plasma performance needs to be understood in order to predict the performance of ITER. Since beryllium is a light impurity ($Z = 4$), similar to carbon ($Z = 6$), the focus of the community is on understanding the significance of the heavy tungsten impurity ($Z = 74$) in core plasma dynamics. In neoclassical theory, the centrifugal force from plasma rotation redistributes heavy impurities to the outboard side of the plasma [115]. When the flow velocity of a species becomes of the same order as its thermal velocity, the centrifugal force becomes significant in the momentum balance equation. This condition is easily achieved for tungsten in JET NBI-heated discharges, where the NBI power exceeds 15 MW and the toroidal rotation velocity is of the order of 10^5 ms^{-1} . The centrifugal force along the magnetic field lines is balanced by the parallel pressure gradient and the parallel electric field, which translates to the poloidal asymmetry of the density of the impurity species. Bolometer and soft X-ray tomographies have often revealed this feature in the recent JET-ILW campaigns. Due to carrying a large number of electrons, tungsten is effective at stopping NBI particles and, therefore, the possibility of a tungsten distribution peaked in the path of the beam, on the outboard side, altering the NBI heat source had to be investigated. The motivation of Publication I was to evaluate the effect of a tungsten distribution, concentrated on the outboard side by the centrifugal force, on the distribution of neutral beam ions in JET plasmas and to assess whether core heating has been affected by the new wall material.

A theoretical model was implemented in ASCOT, based on the work of J. Wesson and M. Romanelli [116]. The model describes the effect of a centrifugal force on the distribution of a heavy trace impurity in a rotating plasma. The model gives an expression for the two-dimensional density profile of impurity I as a function of flux-surface averaged quantities that

can be obtained from a one-dimensional transport simulation,

$$n_I(\psi, \theta) = \langle n_I(\psi, \theta) \rangle \frac{\exp\left(\frac{m^* \omega^2(\psi)}{2T_i(\psi)} R^2(\psi, \theta)\right)}{\left\langle \exp\left(\frac{m^* \omega^2(\psi)}{2T_i(\psi)} R^2(\psi, \theta)\right) \right\rangle}, \quad (4.1)$$

where n_I is the impurity density, $\langle f \rangle$ denotes the flux-surface average of f , $m^* = m_I - Zm_i T_e / (T_e + T_i)$, T_i and T_e are the ion and electron temperatures, respectively, Z is the charge state of the impurity, R is the major radius and ω is the angular frequency of plasma rotation. Equation (4.1) produces an up-down symmetric density distribution that is peaked at the outer midplane, illustrated in Figure 4.1, which qualitatively corresponds to experimental observations [117]. The impurity density is redistributed along flux surfaces but no cross-field transport is induced. The model was validated by comparing its predictions to soft X-ray and bolometry measurements in JET ILW discharges. A JINTRAC transport simulation was carried out to obtain the flux-surface averaged density profiles of all ionization states of tungsten that were then mapped to 2D a posteriori, using a post-processing program SXRPY, developed for this work. The predicted radiation profile was calculated from the 2D density profile and compared with the radiation measurements. The transport coefficients of tungsten were adjusted iteratively until a match to the radiation measurements was obtained. Once the correct transport coefficients for tungsten were found, a coupled JINTRAC-ASCOT run was launched.

The hypothesis was that the peak of tungsten on the outer midplane would have a strong interaction with the incoming neutral beam. In the ASCOT simulations, an interaction was seen to shift the beam deposition off-axis, but the interaction was found to be relatively weak. Changes of the order of 5 % in the ionization source and 10 % in beam ion density and heat deposition profiles were found in the simulations when using a realistic tungsten concentration, based on two JET ILW discharges. The tungsten peak did, however, increase the pitch angle scattering of trapped particles near the separatrix, scattering them to passing orbits and, hence, increasing the fast ion density on the HFS. This is seen as a change in the velocity space distribution of the fast ions near the tungsten peak, as indicated in Figure 4.2.

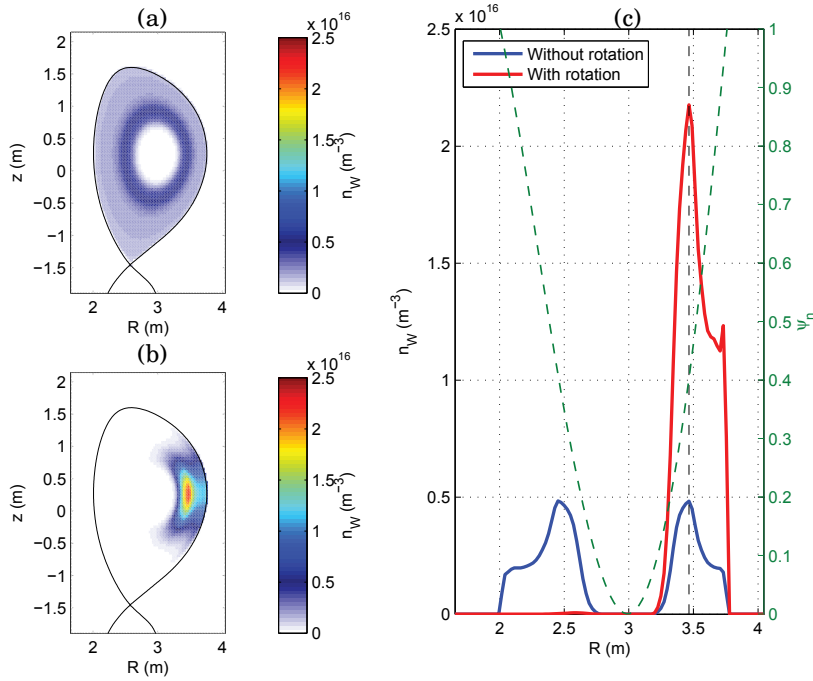


Figure 4.1. Total tungsten density profile from the JINTRAC simulation of JET discharge 82794 at 45.3 s mapped to 2D **(a)** assuming uniform distribution on flux surfaces, and **(b)** with the effect of the centrifugal force described by Equation (4.1). Figure **(c)** shows the midplane cross-sections of **(a)** and **(b)**, overlaid with the normalized poloidal flux coordinate ψ_n indicated by the green dashed line. The black dashed line marks the position of the tungsten density peak.

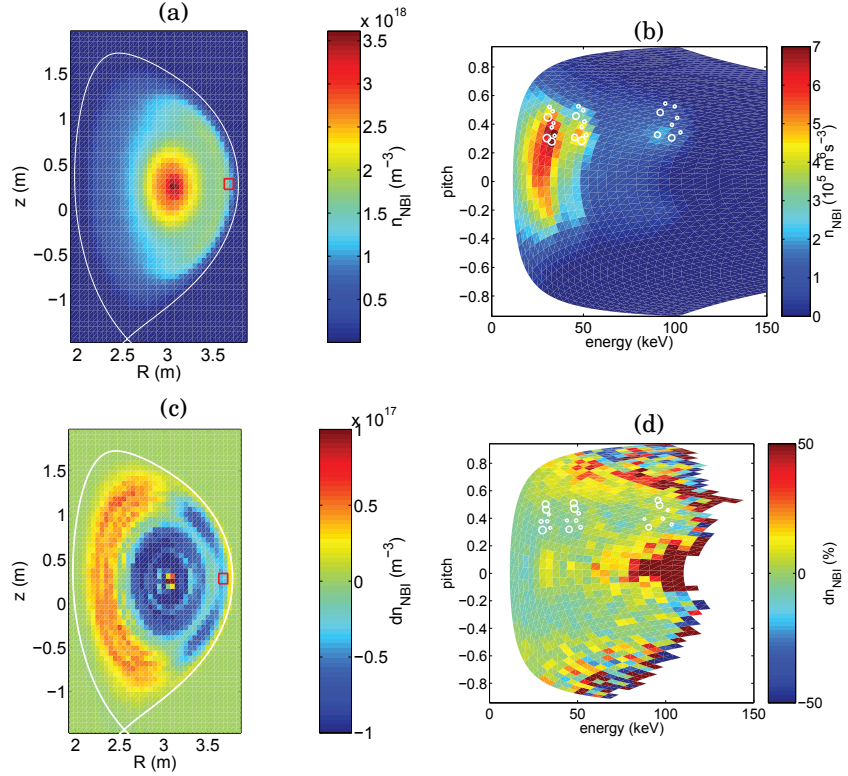


Figure 4.2. The NBI slowing-down density distribution in JET discharge 82722 at 5.9s **(a)** in (R, z) space and in **(b)** (ξ, W) space, averaged in (R, z) space over the red box in panel **(a)**. Panels **(c)** and **(d)** show the relative change in **(a)** and **(b)**, respectively, when the redistribution of tungsten by the centrifugal effect is taken into account. The ionization sources are depicted by white circles in **(b)** and **(d)** whose size represents the source magnitude. During slowing down, particles move down (to the left) in energy and scatter (up and down) in pitch. The relative change of density **(d)** shows that pitch scattering increases when the centrifugal force is included. The distribution spreads to a wider range of pitch angles and the density close to the sources decreases.

4.1.2 Modelling of local CTS measurements of fast ion density in TEXTOR

As was discussed in Section 3.4, measuring the distribution of confined fast ions is much more difficult than measuring fast ion losses. The CTS diagnostic, introduced in Section 3.4, is one of the few diagnostics available that can directly measure the confined fast ion distribution. It is capable of locally measuring the high energy tails of the fast ion phase space density along a selected pitch angle. The motivation of Publication II was to show that ASCOT can accurately model the confined fast ion distribution by comparing it with CTS measurements on the TEXTOR tokamak. The simulations were repeated with the VENUS code [118], to verify the results and benchmark the two codes.

Fast NBI ions were simulated with ASCOT in four TEXTOR discharges 111506, 111508, 111509 and 111512 that were similar in terms of plasma parameters, but the CTS diagnostics was aimed at a different plasma volume in each discharge. The set-up of the measurement volumes is illustrated in Figure 4.3(a). The four measurement volumes were chosen so that measurements were taken at two different major radii, $R_{ax} \approx 1.8$ m (on-axis) and $R_{off-ax} \approx 2.0$ m (off-axis), and two different toroidal angles. Since the angle between the detector and the measurement volume determines the pitch angle onto which the fast ion velocity space distribution is projected, the projections on two pitch values, $\xi_1 \approx -0.35$ and $\xi_2 \approx -0.75$ (corresponding to the pitch angles 110° and 140° , respectively), were obtained at both R_{ax} and R_{off-ax} . A 2D plasma equilibrium calculated by the DIVA equilibrium code [119] for discharge 11508, illustrated in Figure 4.3(a) was adapted to ASCOT and used as the magnetic background for all discharges. The radial plasma density and temperature profiles from Thomson scattering and charge exchange diagnostics are displayed in Figure 4.3(b), along with the q -profile.

A 4-dimensional fast ion phase-space density distribution $f(R, z, v_{\parallel}, v_{\perp})$ was calculated by ASCOT for each discharge. The velocity distributions, averaged over the four measurement volumes of the CTS diagnostic, are displayed in Figure 4.4. Synthetic CTS measurements are obtained by projecting the distribution on the red and cyan dashed lines.

The comparison presented in Publication II found good agreement between the codes and the on-axis measurements. The off-axis densities predicted by ASCOT and VENUS underestimated the measured density

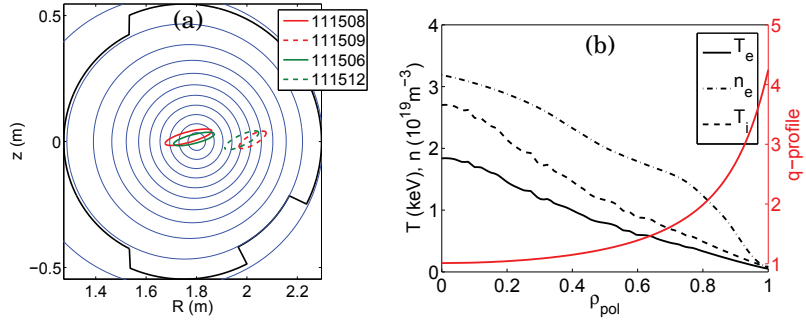


Figure 4.3. The model of the poloidal cross-section of TEXTOR (a) with the limiter surface shown by the black curve, the flux surfaces by the blue contours and the measurement volumes of CTS in the four studied discharges by the red and green curves. Plasma profiles of ion and electron temperature and electron density in TEXTOR discharge 111506 (b). Ion density is assumed equal to electron density.

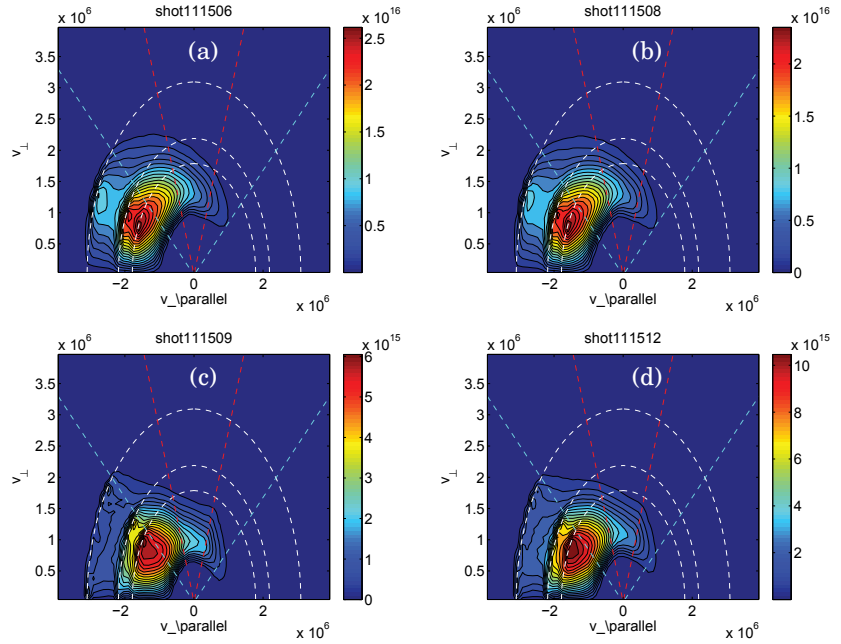


Figure 4.4. The simulated 2D velocity distributions of the NBI ions, averaged over the measurement volume, in TEXTOR discharges (a) 111506 (b) 111508 (c) 111509 and (d) 111512. White dashed lines show the velocity contours corresponding to the birth energies of beam ions (W_0 , $W_0/2$, $W_0/3$), where W_0 is the full beam energy. Red and cyan dashed lines show the contours of pitch $\xi = -0.35$ and $\xi = -0.75$ on which the distribution is projected in Publication II, respectively.

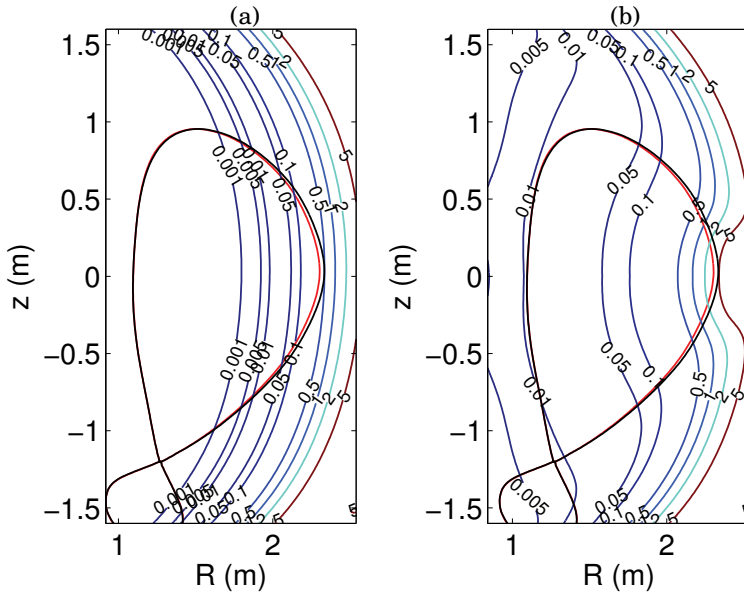


Figure 4.5. Contours of the ripple strength in DIII-D according to Equation (2.11), in percentage, without the TBM mock-up (a) and with the TBM mock-up (b). The last closed flux surface is shown in red for discharge 140144 and in black for discharge 140156.

significantly. The reason for the discrepancy was not found within the scope of the paper, but fast ion redistribution due to MHD activity was suspected. ASCOT and VENUS were successfully benchmarked against each other and improvements were made to the Coulomb collision models of the codes based on the issues resolved during the study.

4.1.3 Fast ion losses in DIII-D TBM mock-up experiments

In 2009, DIII-D performed experiments dedicated to investigating the effect of a TBM-like perturbation on various aspects of tokamak performance [53]. The perturbation was generated by a mock-up set of coils installed into the machine. Publication III was part of a concentrated effort to benchmark fast ion codes capable of treating 3D magnetic fields for ITER simulations. The aim of the study was to calculate the footprint of the fast ion heat load on the tiles protecting the TBM mock-up module, which could be compared to thermocouple measurements on the back of the tile.

Two DIII-D discharges, 140144 and 140156, with different outer plasma-wall gaps, 5cm and 8cm, respectively, were studied with ASCOT. Both pulses had 5.8 MW of NBI heating. The perturbation due to the TBM

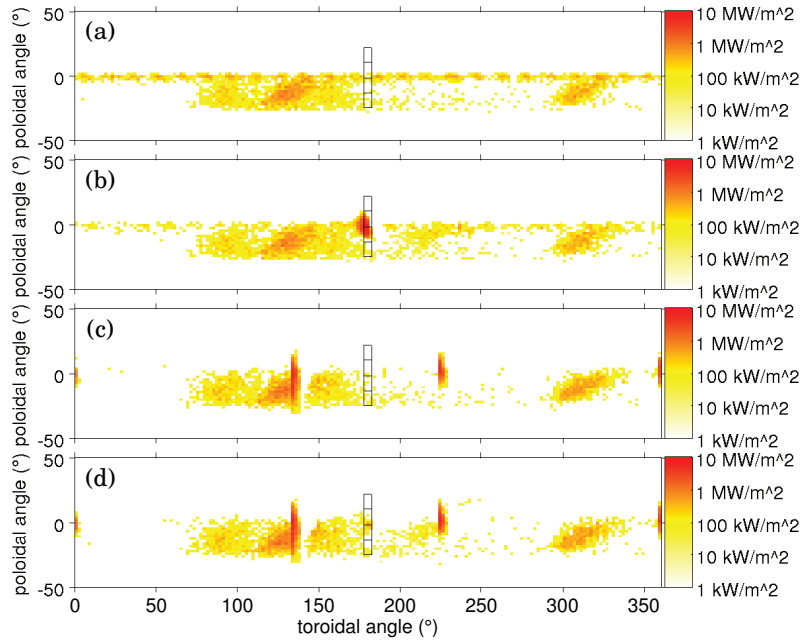


Figure 4.6. Simulated lost fast ion power flux distribution on the first wall in DIII-D discharge 140144. The TBM mock-up module is located at the toroidal angle of 180° and the tiles protecting it are outlined in black. The power load is calculated on an axisymmetric first wall with the TBM-mock up off in (a) and on in (b). The power load is calculated on a 3D wall model with three limiters at 0° , 135° and 225° , with the TBM-mock up off in (c) and on in (d).

mock-up was calculated with a Biot-Savart solver in the vacuum approximation and combined to the magnetic field ripple calculated from DIII-D TF coil currents. The perturbation magnitude, calculated with the definition of TF ripple from Equation (2.11) is illustrated in Figure 4.5.

In the experiment, the TBM mock-up module was shadowed by two poloidal wall limiters, separated by 45° in toroidal angle. The importance of including the limiters in the simulation model was found essential to accurately simulate the wall power loads in Publication III. ASCOT was the only code available with the inbuilt ability to facilitate arbitrary 3D wall structures. The effect of limiters is clearly seen in the simulation results in Figure 4.6. In the model without limiters, a bright hot spot appears on top of TBM tiles 2 and 3 when the perturbation field is on. With the rectangular limiters included, the hot spot shrinks and the magnitude of the peak power flux is lower.

The results of Publication III were compared to three other codes: OFMC [43], SPIRAL [120] and DELTA5D [121]. Good agreement was found between ASCOT, OFMC and SPIRAL, when full-orbit tracing was used in ASCOT

and realistic limiter models were introduced in all codes [54]. With guiding center following, ASCOT underestimated the heat loads by roughly NUMBER %. Heat conduction calculations, based on the the fast ion loss simulations, were in quantitative agreement with thermocouple temperature measurements taken behind the tiles shielding the TBM mock-up module.

In addition, the confinement of 1.01 MeV tritons born in DD fusion was studied experimentally by using the 14 MeV DT neutron flux as a proxy for the confinement of tritons. A reduction of 30 % in the neutron rate was observed when the TBM mock-up was switched on, which was credited to losses of fusion products [53]. The birth and losses of DD tritons were also simulated with ASCOT and the reduction of 30 % in confined tritons was reproduced by full-orbit simulations.

4.2 Predictions of fast ion wall loads in ITER

All ITER analyses presented in this section have been performed for two ITER standard operating scenarios, the 15 MA and the 9 MA scenario [122]. The 15 MA inductive ELMy H-mode scenario will most likely be the standard operating scenario at the start of ITER operation due to the vast experience base of operating such scenarios on existing tokamaks. However, satisfactory ELM mitigation techniques need to be developed for sustained operation [22]. Kinetic plasma profiles for the 15 MA scenario, simulated with the ASTRA code [62], are presented in Figure 4.7(a). The 15 MA scenario is also the most likely scenario to produce a fusion gain of $Q = 10$ with a total fusion power of 500 MW. According to Equation (1.3), 100 MW of the power is carried via alpha particles and the rest via neutrons.

The 9 MA scenario is an advanced operating scenario developed for steady-state operation [123]. The plasma current is driven non-inductively by a combination of non-inductive current drive and a high bootstrap current fraction, achieved by reversing the central shear of the q -profile. A q -profile with reversed shear has been found to stabilize turbulence and create an Internal Transport Barrier (ITB), that allows maintaining a high plasma pressure at a reduced plasma current [124], but also leads to an accumulation of heavy impurities. Kinetic profiles simulated for the 9 MA scenario with ASTRA are shown in Figure 4.7(b). The temperature and density pedestals are lower than in the 15 MA scenario, but the core

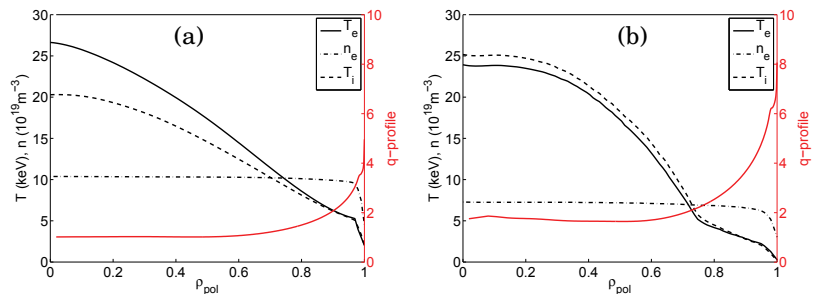


Figure 4.7. Radial profiles of temperature and density calculated by the ASTRA code in (a) the ITER 15 MA H-mode scenario and in (b) the ITER 9 MA advanced scenario.

temperature is recovered by the ITB, and even exceeds the ion temperature in the 15 MA scenario on the magnetic axis. A fusion gain of $Q = 6$ is projected for the 9 MA scenario, due to its weaker pedestal and higher need for auxiliary heating.

In the ASCOT simulations reported in Publication IV, the use of ferritic inserts was found to be an effective way of mitigating fast ion losses due to TF ripple in ITER. The losses of NBI ions, ICRH ions and alpha particles due to toroidal field ripple were calculated in the ITER standard operating scenarios. A preliminary investigation into the losses due to TBMs was also reported in the publication, but the treatment of the perturbed field created by the TBM was later discovered to be inaccurate. Results with a proper treatment of the TBM perturbations are given in Section 4.2.2, where the effect of TBMs was found negligible. The ASCOT simulations were extended to include the combined effect of ripple, TBMs and ELM control coils in Publication V.

4.2.1 Fast ion losses due to toroidal field ripple

A toroidal field ripple above 1 % is expected in ITER [15] because of its large major radius (6.2 m) and relatively small number of TF coils (18), as shown in Figure 4.8(a). A large TF ripple may cause localised losses of fast particles as was discussed in Section 2.2.1. However, with ferritic compensation the ripple can be mitigated down to 0.2 % on the separatrix, as shown in Figure 4.8(b). The motivation of publication Publication IV was to calculate the losses of fast ions in ITER due to TF ripple and to evaluate the effectiveness of ripple mitigation by ferritic inserts.

Three fast ion sources were considered, alpha particles from thermal DT-fusion and fast deuterium ions from both NBI injection and ICRH ac-

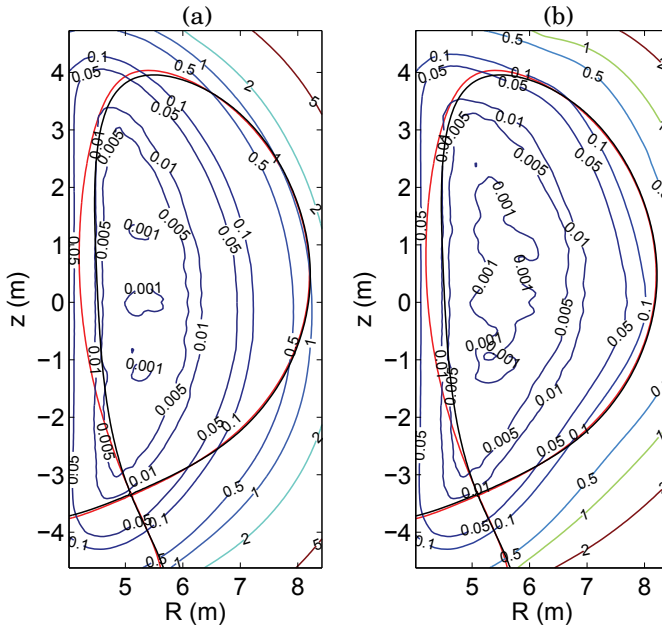


Figure 4.8. Contours of the ripple strength according to Equation (2.11) in ITER, unmitigated (a) and with ferritic inserts (b). The last closed flux surface is shown in red for the 15 MA scenario and in black for the 9 MA scenario.

celeration. Fast alpha particles are born in DT fusion reactions as discussed in Section 3.1.3. The two operating scenarios considered were the 15 MA ELMy H-Mode scenario, denoted “Scenario-2” in the publication, and the 9 MA advanced steady-state scenario, denoted “Scenario-4” in the publication.

The first wall design of ITER has been in a state of constant change throughout this thesis project. At the time of Publication IV, the design was to insert poloidal limiters in two opposite equatorial ports. In order to facilitate this design, ASCOT was upgraded with a fully 3D wall model that describes the wall tiles as triangular or rectangular polygons. Intersections of particle trajectories with the wall are calculated with an optimized ray-tracing algorithm [125]. Changes to the design of the wall have been found to change the footprint of the losses, as protruding elements tend to receive most of the power, but the total lost power flux [126] is independent of the wall design.

The main results of the study are summarized in Figure 4.9. It was found that fast ion losses due to the uncompensated ripple will lead to peak power fluxes of 1.6 MW/m^2 in the 9 MA scenario and 0.7 MW/m^2 in the 15 MA scenario on the first wall. The majority of the power flux

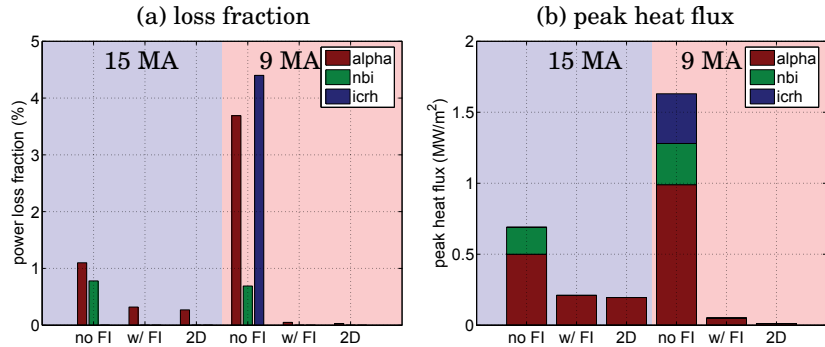


Figure 4.9. Summary of the ripple loss calculations of **alpha particles**, **NBI ions** and **ICRH-accelerated ions** in the **15 MA scenario** and the **9 MA scenario** reported in Publication IV. Panel (a) shows the lost fraction of the total fast ion power and panel (b) shows the peak power load on the surface of the first wall. The losses due to the uncompensated ripple (no-FI) are mitigated almost to the level of axisymmetry (no ripple) by the ferritic inserts (with FI). The FI's reduce the 0.7 MW/m^2 peak heat load by a factor 3 in the 15 MA scenario, and the 1.6 MW/m^2 peak heat load by two orders of magnitude in the 9 MA scenario.

consists of lost alpha particles. Less than 1% of NBI power is lost in both scenarios, while ICRH losses are only seen in the 9 MA scenario. However, the high power flux can be very effectively reduced by ferritic inserts. According to the modelling, the power loads are reduced by a factor of 3 in the 15 MA scenario, and by up to a factor of 100 in the 9 MA scenario. The difference is due to the following: The 9 MA scenario responds much more strongly to the ripple mitigation than the 15 MA scenario. Due to low density and temperature at the pedestal top in the 9 MA scenario, seen in Figure 4.7(b), the fast particle sources are deep in the core plasma. However, since the plasma current is only 9 MA, trapped fast particles have wider orbits and the ripple diffusion step size is larger. The unmitigated ripple can reach the fast ions born in the core and cause large losses, while the mitigated ripple acts only in the edge where no fast particles are born.

The footprint of the fast ion power load on the wall is dominantly on the poloidal limiters. Figure 4.10 illustrates the distribution of the heat load carried by lost alpha particles in the 15 MA scenario on the first wall components. The leading edges of the limiters absorb approximately 75 % of the lost alpha power. The rest is distributed evenly between the divertor (in the bottom of the figure) and below the poloidal midplane in the area between the limiters, where the first wall tiles come closest to the plasma. In this region the footprint of the 18-fold symmetry of the ripple can be observed.

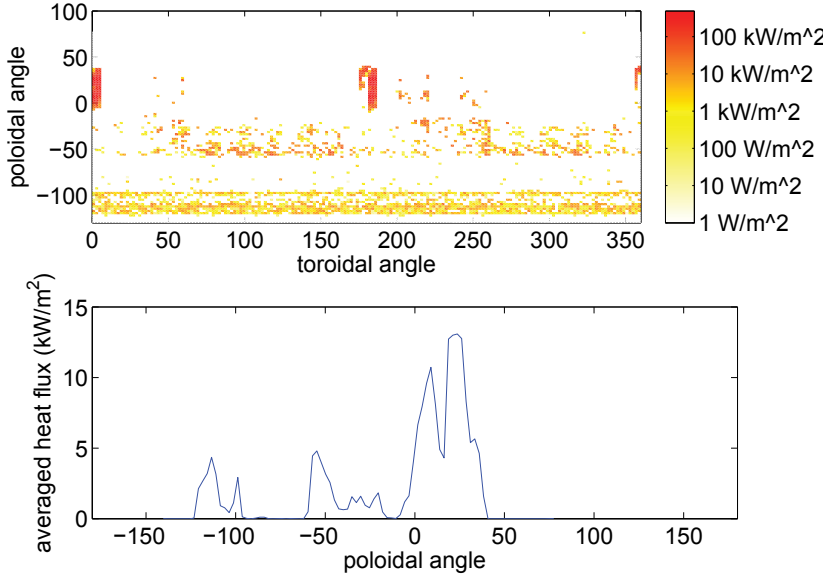


Figure 4.10. The distribution of heat flux to the first wall due to alpha particle losses in the 15 MA scenario with uncompensated ripple. In the top panel, the power load is distributed onto a grid in toroidal and poloidal angle. The two port limiters, at $\phi = 0^\circ$ and $\phi = 180^\circ$, absorb most of the heat flux. The rest of the losses are deposited below the outer midplane ($\theta \approx -50^\circ$) and in the divertor ($\theta \approx -100^\circ$). In the bottom panel, the power load distribution from the top panel is averaged over the toroidal angle. The toroidally averaged heat flux peaks on the port limiters (above $\theta = 0^\circ$) and the losses at $\theta \approx 50^\circ$ and $\theta \approx 100^\circ$ are identifiable as smaller peaks.

4.2.2 Fast ion losses due to test blanket modules

In addition to ripple losses, Publication IV also addressed the fast ion losses due to the nonperiodic perturbations due to the TBMs in ITER for the first time. This was done by including the perturbation due to the magnetization of the ferritic material in the TBM to the 3D magnetic fields used by ASCOT. As was discussed before in Section 2.2.2, ITER will have six TBMs located in three midplane ports. The TBMs are used for tritium breeding and due to the neutron irradiation must contain large amounts of ferritic steel that becomes magnetized in the magnetic field of the tokamak. The magnetic perturbations due to the TBMs were calculated assuming magnetization from the dominant toroidal field component only for Publication IV. Under that approximation, the TBMs were found to destabilize passing orbits, in a manner similar to the stochastic ripple diffusion of trapped orbits, by inflicting a radial “kick” on the particles whenever they passed close to the TBM. The result of including the FI-compensated ripple and the TBMs in the ASCOT simulations are summarized in the first bars, denoted “RIPLOS”, in Figure 4.11, for both scenarios. Significant additional losses of NBI ions in the 15 MA scenario and ICRH ions in the 9 MA scenario were predicted. The power was deposited mostly on the divertor, where it is spread evenly on a large area and the peak heat loads remained below 1 MW/m^2 . The results indicated an ergodic nature of particle orbits and formation of drift islands in non-periodically perturbed fields [52].

However, the approximations made in the calculation of the perturbed field due to the TBM in Publication IV were later found to be too crude. The magnetic field due to magnetization of a ferritic material by an external magnetic field must always be exactly parallel to the external field, i.e., the ferritic material changes the magnitude of the field, not its direction. In the calculation of the magnetization of the TBMs for Publication IV, the TBM perturbation field was purely toroidal and, thus, the perturbations were not aligned with the poloidal field. The misalignment led to an overestimation of the radial “kicks” received by the particles as they passed the TBM by an order of magnitude [127].

After the error was discovered, the magnetization of the TBMs was recalculated using the total magnetic field, the effect of the TBMs on fast ion losses was not found to be significant. The TBM magnetization was first calculated for OFMC calculations for the 9 MA scenario [128, 129],

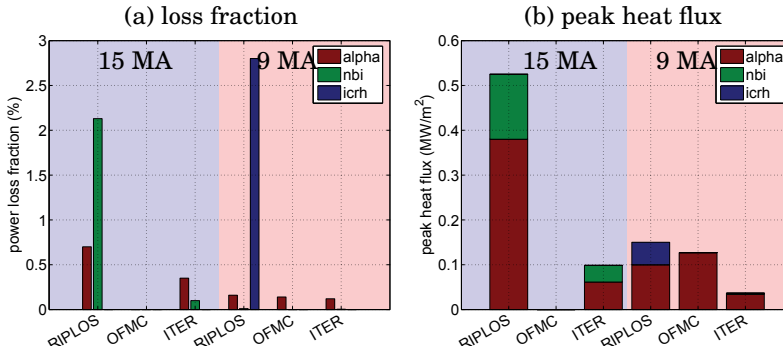


Figure 4.11. Summary of the TBM loss calculations of **alpha particles**, **NBI ions** and **ICRH-accelerated ions** in the **15 MA scenario** and the **9 MA scenario**. In **(a)** the lost fraction of the total fast ion power, and in **(b)** the peak power load on the surface of the first wall. The losses reported in Publication IV (RIPLOS) are overestimations due to oversimplification in the modelling of the perturbation. The losses calculated with the magnetic backgrounds from ITER are not significantly different from the losses with ripple and the FI's in Figure 4.9.

and later by commission of ITER for both scenarios [130]. The latter calculation also took into account the toroidally asymmetric distribution of ferritic inserts around neutral beam ports in ITER. ASCOT simulations of alpha particle and NBI losses were carried out using these magnetic backgrounds and the results are summarized in Figure 4.11, with bars labeled “OFMC” and “ITER”, respectively. The TBMs were not found to add significant additional losses compared to the previous results with FI-compensated ripple, even though the local perturbations of the TBMs are of similar magnitude to the uncompensated periodic ripple ($\delta \approx 1\%$). The results of Publication IV were found to clearly overestimate the effect of the TBMs, due to the reason outlined above. Fortunately for ITER, the 1 % TBM perturbation is much lower than what was applied in the DIII-D TBM mock-up experiments (5 %, recall Figure 4.5). Therefore, no hot spots on the first wall due to TBMs are predicted for ITER, contrary to the DIII-D results reported in Publication III.

4.2.3 Fast ion losses due to ELM control coils

In Publication IV, as well as in more recent studies [71, 129], it has been shown that a non-axisymmetric magnetic field can lead to losses of fast ions in ITER. However, the simulations agreed that the total fast ion loss fraction was likely to remain small and the research was more concentrated on identifying possible hot spots on the first wall. However, in

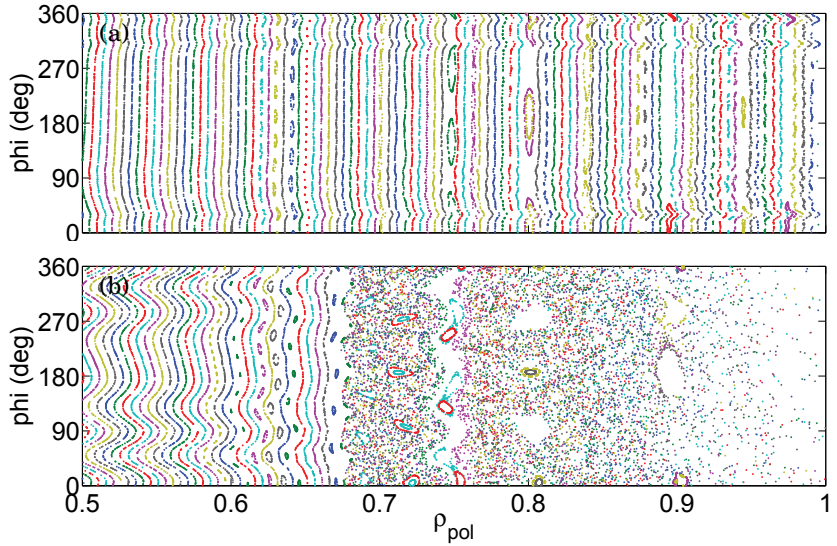


Figure 4.12. The ergodization of field lines due to the ECCs with the 90 kAt $N = 4$ waveform in the 15 MA scenario. Poincaré plots, calculated by vacuum field line tracing, of field lines crossing the outer midplane with the ripple and TBMs only (a) and ripple, TBMs and ECCs (b) show the formation of magnetic islands and a wide ergodic layer when the ECCs are activated.

2012, Tani et. al. [131] and Shinohara et. al. [132] reported OFMC calculations of losses of over 20 % of NBI power in the presence of ELM control coils in ITER. The motivation of Publication V was to reproduce these results with ASCOT, and to investigate the physical mechanisms behind the unexpectedly large losses.

The vacuum field of the ELM Control Coils (ECCs) was found to create wide layers of stochastic field lines deep inside the pedestal. The calculations were done using parts of the newly developed ASCOT4 suite. The vacuum 3D magnetic field was calculated with the Biot-Savart law integrator code BioSaw and the field line tracing was carried out with the FILIP field line tracing code. The field line structure is illustrated by Poincaré plots in Figure 4.12. The large losses reported in [131] were reproduced, and the results of [132] were shown to be sensitive to the relative phases of the coil currents.

The main result, however, was pointing out the inconsistency in the background magnetic field model. If the ergodization of the magnetic field was accurately described by the vacuum modelling, it would cause a rapid pump-out of the bulk plasma density since field lines in the ergodic layer are connect to the divertor. In the absence of thermal plasma, the fast particle sources in the ergodic layer would be reduced to zero, and there

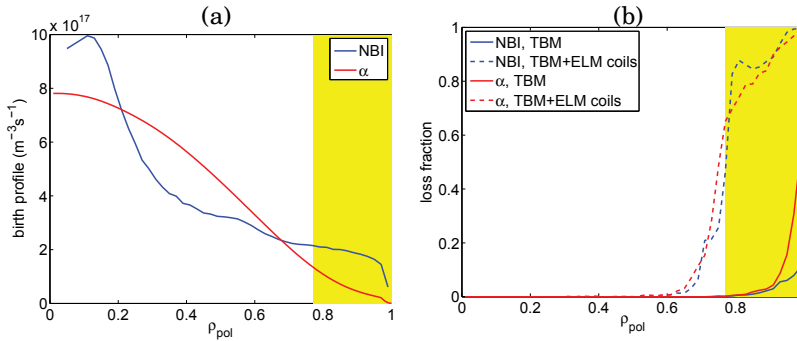


Figure 4.13. The density of alpha particles and NBI ions born per flux surface (a) and the fraction that is lost (b) with and without the ELM coils (dashed and solid lines, respectively) in the 15 MA scenario. There is a sharp rise in losses when the ECCs are activated, which aligns with the edge of the ergodic field layer, indicated by the yellow shaded area. However, such an ergodic layer would cause a density pump-out that is not accounted for by the model, effectively reducing the fast ion sources (a) in that region to zero. The loss of density from $\rho \geq 0.8$ would be catastrophic for the plasma performance rendering the fast ion confinement irrelevant.

would be no additional losses. This is illustrated in Figure 4.13. Such a loss of density would, of course, be catastrophic for plasma performance and most likely lead to the termination of the discharge. Fortunately, recent studies have shown that the ECC fields will be strongly damped inside the pedestal top [133] by the plasma response to the perturbation. The ergodic layer is restricted to the steep gradient region ($\psi_n > 0.96$), where ergodization is needed for ELM mitigation. If this is the case, additional fast ion losses are likely to remain small.

The ASCOT4 results were exhaustively benchmarked with OFMC calculations [131, 132], within the framework of the ITPA working group on energetic particles after the publication of Publication V, and a good agreement was found. We can conclude that the reported OFMC results are consistent with the vacuum field approximation, but in this case, the vacuum field modelling does not give reliable physics results.

5. Summary and Future Prospects

The confinement of fast ions is essential for the successful operation of ITER and future fusion power plants. Confined fast ions are needed for heating the plasma to the temperature needed for the fusion burn and, on the other hand, even a small fraction of fast ion losses may cause significant structural damage, e.g., melting, to the plasma facing components of the reactor. Fast ions are well confined in an axisymmetric toroidal magnetic field with a sufficiently large poloidal field component but, unfortunately, the magnetic axisymmetry is broken in ITER due to several structural error field sources. The confinement of fast ions in a complex 3D magnetic topology can only be predicted by massive Monte Carlo simulations that follow the trajectories of the particles in the domain of the entire vessel throughout their lifetime that is of the order 1 s in ITER. In this thesis, state-of-the-art numerical fast ion simulations of ITER and existing tokamaks have been presented. The simulations have been performed with the ASCOT code, developed at Aalto University School of Science and VTT Technical Research Centre of Finland. Over the course of this thesis, ASCOT was developed and modernized into a fully 3D fast ion modelling tool.

The elementary theory of charged particle motion in axisymmetric toroidal magnetic fields was presented in Chapter 2. In the absence of collisions, the orbits of charged particles in tokamaks can be categorized into passing and trapped orbits, both of which remain confined in axisymmetric fields. However, collisions with the background plasma cause particles to undergo a random walk in velocity space that creates diffusion in real space, which can lead to losses. When the axisymmetric magnetic field is perturbed, additional loss channels appear. Toroidal Field ripple, due to the finite number of toroidal field coils, traps a small fraction of particles in ripple wells but, more importantly, causes stochastic diffusion of colli-

sionless trapped orbits. Non-periodic perturbations, such as those due to ferritic materials or in-vessel coils, reconnect magnetic field lines, giving rise to islands or ergodic layers that degrade confinement.

Chapter 3 summarized the ASCOT code and its coupling to transport codes via the JINTRAC suite. On its own, the ASCOT code is a versatile tool for the kinetic modelling of minority ion species in steady-state conditions in a realistic tokamak geometry, given kinetic plasma profiles measured or predicted by other codes. The implementation of a 3D magnetic field and vessel geometry enables ASCOT to model fast particle physics in great detail. Small asymmetries in the magnetic field, such as the TF ripple, can be modelled and have been found to play a large part in fast ion losses. When coupled with a transport code, ASCOT can be used to simulate the dynamics of fast ions in NBI or alpha particle heated plasmas.

In the results presented in Chapter 4, ASCOT has been used for interpretive modelling of existing tokamaks and predictive modelling of ITER. In Publications I and II ASCOT simulations of confined fast ions were successfully compared to neutron camera measurements at JET and CTS measurements at TEXTOR. The ASCOT simulations of fast ion losses reported in Publication III were benchmarked to other prominent 3D fast ion codes in the fusion community and to thermocouple measurements in DIII-D [54]. In Publication IV, ASCOT was used to predict the losses of alpha particles, NBI ions and ICRH ions in the presence of TF ripple and TBMs in ITER. It was found that the natural $\sim 1\%$ TF ripple from the 18 TF coils in ITER will give rise to unacceptable fast ion heat loads that jeopardize the integrity of the plasma facing surface of the first wall. However, the simulations also revealed that by mitigating the ripple with ferritic inserts down to 0.3% , the fast ion losses are reduced almost to the axisymmetric level. The TBMs were found to destabilize passing orbits and lead to losses of NBI and ICRH ions. However, the approximations made in calculating the magnetization of the TBMs in Publication IV were later found to be too crude, and the revised results presented in Section 4.2.2 show the TBMs do not significantly increase fast ion losses. In Publication V the error fields induced by the ELM control coils in ITER were found to lead to large losses of NBI ions and alpha particles. However, it was shown that the vacuum field approximation, widely used by the fast ion modelling community at the time, was not applicable, since the magnetic perturbation will be damped by the plasma response inside

the pedestal in ITER.

The final answer to fast ion losses would require a self-consistent model of the plasma equilibrium, the thermal plasma transport, the magnetization of machine materials, currents in the machine and the fast ions. Such a model would be extremely impractical to solve on today's computers, but steps are being taken towards more consistent modelling. The most important piece of the puzzle is the response of the thermal plasma to the external magnetic perturbations, as was pointed out in Publication V. A project commissioned by Fusion for Energy is underway at Aalto University to calculate the vacuum 3D magnetic field in ITER, starting from the CAD drawings of machine components, and to calculate the appropriate plasma response field to the 3D perturbations. The total field will then be used in ASCOT to resolve the real fast ion losses. The JINTRAC suite of codes is currently being updated to become a portable tool for tokamak plasma transport simulations, with ITER and DEMO being the most interesting subjects of study. Ripple will, again, be an issue in DEMO and ASCOT/JINTRAC would be an excellent tool to evaluate the risks posed by it. At JET, the upcoming DT campaign in 2017 will provide new opportunities for ASCOT fast ion loss calculations with JINTRAC, for example investigating the discrepancy between predicted and measured neutron rates [134].

Acknowledgements

The author of this thesis would like to thank the Vaisala fund of the Finnish Academy of Sciences and Letters for their financial support over two years of the thesis work. Tekniikan Edistämissäätiö (TES) and the Fortum foundation are also gratefully acknowledged for their financial support. Parts of this thesis work have been funded by the Academy of Finland projects No. 121371, 134924 and 259675. Many supercomputing centres have contributed valuable computing time for the development and execution of ASCOT. The author would like to acknowledge the support of the following institutes: HPC-FF, the HELIOS supercomputer system at International Fusion Energy Research Centre, Aomori, Japan, under the Broader Approach collaboration between Euratom and Japan, implemented by Fusion for Energy and JAEA, the Aalto Science-IT project, and the supercomputing resources of CSC - IT center for science.

Errata

Publication III

The toroidal locations of the limiters should be 0deg, 135deg and 225deg

Publication IV

The value for the peak power flux for scenario-2 no-ripple in table 1 has been misprinted. The correct value is 195 kWm^{-2} . The other values in the table are correct.

Publication V

Equation (1) is incorrect. It should be written as Equation (3.6) of this thesis.

Bibliography

- [1] Bethe, H. A., Phys. Rev. **55** (1939) 434.
- [2] Smith, C. L. and Cowley, S., Philosophical Transactions of the Royal Society A: Mathematical, Physical and Engineering Sciences **368** (2010) 1091.
- [3] Huba, J. D., NRL Plasma Formulary, Naval Research Laboratory, Washington, D.C., 2006.
- [4] Wesson, J., *Tokamaks*, volume 48 of *The Oxford Engineering Science Series*, Clarendon Press, 2nd edition, 1997.
- [5] Kikuchi, M., K., L., and Q., T. M., *Fusion Physics*, International Atomic Energy Agency, 2012.
- [6] Artsimovich, L., Nuclear Fusion **12** (1972) 215.
- [7] Braginskii, S., Reviews of plasma physics **1** (1965) 205.
- [8] Helander, P. and Sigmar, D. J., Collisional Transport in Magnetized Plasmas, by Per Helander, Dieter J. Sigmar, Cambridge, UK: Cambridge University Press, 2005 **1** (2005).
- [9] Garbet, X., Idomura, Y., Villard, L., and Watanabe, T., Nuclear Fusion **50** (2010) 043002.
- [10] Wootton, A. J., Carreras, B. A., Matsumoto, H., et al., Physics of Fluids B: Plasma Physics (1989-1993) **2** (1990) 2879.
- [11] Wagner, F., Becker, G., Behringer, K., et al., Phys. Rev. Lett. **49** (1982) 1408.
- [12] Zohm, H., Plasma Physics and Controlled Fusion **38** (1996) 105.
- [13] Suttrop, W., Plasma Physics and Controlled Fusion **42** (2000) A1.
- [14] ITER web page, <http://www.iter.org/>, 2014.
- [15] ITER Physics Expert Group on Energetic Particles, H., Drive, C., and Editors, I. P. B., Nuclear Fusion **39** (1999) 2471.
- [16] Hawryluk, R. J., Batha, S., Blanchard, W., et al., Physics of Plasmas (1994-present) **5** (1998) 1577.
- [17] Keilhacker, M., Gibson, A., Gormezano, C., et al., Nuclear Fusion **39** (1999) 209.

- [18] Zweben, S., Budny, R., Darrow, D., et al., Nuclear Fusion **40** (2000) 91.
- [19] Federici, G., Loarte, A., and Strohmayer, G., Plasma Physics and Controlled Fusion **45** (2003) 1523.
- [20] Loarte, A., Saibene, G., Sartori, R., et al., Plasma Physics and Controlled Fusion **45** (2003) 1549.
- [21] Loarte, A., Lipschultz, B., Kukushkin, A., et al., Nuclear Fusion **47** (2007) S203.
- [22] Loarte, A., Huijsmans, G., Futatani, S., et al., Nuclear Fusion **54** (2014) 033007.
- [23] Suttrop, W., Eich, T., Fuchs, J., et al., Phys. Rev. Lett. **106** (2011) 225004.
- [24] Evans, T., Fenstermacher, M., Moyer, R., et al., Nuclear Fusion **48** (2008) 024002.
- [25] Liang, Y., Koslowski, H. R., Thomas, P. R., et al., Plasma Physics and Controlled Fusion **49** (2007) B581.
- [26] Callen, J., Nuclear Fusion **51** (2011) 094026.
- [27] Heikkinen, J. A. and Sipilä, S. K., Physics of Plasmas **2** (1995) 3724.
- [28] Kurki-Suonio, T., Asunta, O., Hellsten, T., et al., Nuclear Fusion **49** (2009) 095001.
- [29] Hirvijoki, E., Asunta, O., Koskela, T., et al., Computer Physics Communications **185** (2014) 1310 .
- [30] Speth, E., Reports on Progress in Physics **52** (1989) 57.
- [31] Jassby, D., Nuclear Fusion **17** (1977) 309.
- [32] Stix, T., Nuclear Fusion **15** (1975) 737.
- [33] Hazeltine, R. D. and Waelbroeck, F. L., *The framework of plasma physics*, volume 100, Perseus Books, 1998.
- [34] Northrop, T. G., *The adiabatic motion of charged particles*, volume 21, Interscience publishers New York, 1963.
- [35] Littlejohn, R., Physics of Fluids (1958-1988) **24** (1981) 1730.
- [36] Littlejohn, R., Journal of Plasma Physics **29** (1983) 111.
- [37] Tao, X., Chan, A., and Brizard, A., Physics of Plasmas **14** (2007) 092107.
- [38] Hirvijoki, E., *Theory and models for Monte Carlo simulations of minority particle populations in tokamak plasmas*, PhD thesis, Aalto University, School of Science, 2014.
- [39] Eriksson, L.-G. and Porcelli, F., Plasma Physics and Controlled Fusion **43** (2001) R145.
- [40] Hauff, T., Pueschel, M. J., Dannert, T., and Jenko, F., Physical Review Letters **102** (2009) 075004.

- [41] Albergante, M., Graves, J. P., Fasoli, A., et al., Plasma Physics and Controlled Fusion **53** (2011) 054002.
- [42] Goldston, R. J., White, R. B., and Boozer, A. H., Phys. Rev. Lett. **47** (1981) 647.
- [43] Tani, K., Azumi, M., Kishimoto, H., and Tamura, S., J. Phys. Soc. Jpn. **50** (1981) 1726.
- [44] Saibene, G., Sartori, R., McDonald, D., et al., Results of the variable toroidal field ripple experiments in jet, in *22nd IAEA Fusion Energy Conference*, 2008.
- [45] Shinohara, K., Sakurai, S., Ishikawa, M., et al., Nuclear Fusion **47** (2007) 997.
- [46] Tobita, K., Nakayama, T., Konovalov, S. V., and Sato, M., Plasma Physics and Controlled Fusion **45** (2003) 133.
- [47] Fasoli, A., Gormenzano, C., Berk, H., et al., Nuclear Fusion **47** (2007) S264.
- [48] Van der Schaaf, B., Tavassoli, F., Fazio, C., et al., Fusion Engineering and Design **69** (2003) 197.
- [49] Giancarli, L., Chuyanov, V., Abdou, M., et al., Fusion Engineering and Design **81** (2006) 393 .
- [50] Salavy, J.-F., Boccaccini, L., Chaudhuri, P., et al., Fusion Engineering and Design **85** (2010) 1896 , Proceedings of the Ninth International Symposium on Fusion Nuclear Technology.
- [51] Oh, D. K., Jhang, H., Lee, D. K., Ku, D. Y., and Cho, S., Fusion Engineering and Design **86** (2011) 127 .
- [52] Koskela, T., Asunta, O., Hynönen, V., et al., Europhysics Conference Abstracts **32D** (2008) P5.001.
- [53] Schaffer, M., Snipes, J., Gohil, P., et al., Nuclear Fusion **51** (2011) 103028.
- [54] Kramer, G., Budny, B., Ellis, R., et al., Nuclear Fusion **51** (2011) 103029.
- [55] Kramer, G., McLean, A., Brooks, N., et al., Nuclear Fusion **53** (2013) 123018.
- [56] Hawryluk, R., Campbell, D., Janeschitz, G., et al., Nuclear Fusion **49** (2009) 065012.
- [57] Chirikov, B. V., Physics reports **52** (1979) 263.
- [58] Kirk, A., Harrison, J., Liu, Y., et al., Physical Review Letters **108** (2012) 255003.
- [59] Schmitz, O., Evans, T., Fenstermacher, M., et al., Nuclear Fusion **54** (2014) 012001.
- [60] Chapman, I., Kirk, A., Saarelma, S., et al., Nuclear Fusion **52** (2012) 123006.

- [61] Cenacchi, G. and Taroni, A., Rapporto ENEA RT/TIB **88** (1988).
- [62] Pereverzev, G. and Yushmanov, P., (2002).
- [63] Hawryluk, R., An empirical approach to tokamak transport, in Coppi, B., Leotta, G., Pfirsch, D., Pozzoli, R., and Sindoni, E., editors, *Physics of Plasmas Close to Thermonuclear Conditions, Volume 1*, volume 1, pp. 19–46, Oxford, UK, 1981, Pergamon Press.
- [64] Romanelli, M., Corrigan, G., Parail, V., et al., Plasma and Fusion Research **9** (2014) 34030231.
- [65] Sipilä, S. and Heikkinen, J., ASCOT: Accelerated simulation of charged particle orbits in a tokamak, Report TKK-F-A698, Helsinki University of Technology, 1992.
- [66] Sipilä, S., *Monte Carlo simulation of charged particle orbits in the presence of radiofrequency waves in tokamak plasmas*, PhD thesis, Helsinki University of Technology, 1997.
- [67] Asunta, O., Hellsten, T., Hynönen, V., et al., Final report on task tw6-tporiplos, Technical report, Fusion for Energy, 2008.
- [68] Hirvijoki, E., Snicker, A., Korpilo, T., et al., Computer Physics Communications **183** (2012) 2589 .
- [69] Miettunen, J., Kurki-Suonio, T., Makkonen, T., et al., Nuclear Fusion **52** (2012) 032001.
- [70] Miettunen, J., Groth, M., Kurki-Suonio, T., et al., Journal of Nuclear Materials **438, Supplement** (2013) S612 , Proceedings of the 20th International Conference on Plasma-Surface Interactions in Controlled Fusion Devices.
- [71] Kurki-Suonio, T., Asunta, O., Hirvijoki, E., et al., Nuclear Fusion **51** (2011) 083041.
- [72] Lao, L., John, H. S., Stambaugh, R., Kellman, A., and Pfeiffer, W., Nuclear fusion **25** (1985) 1611.
- [73] Hynönen, V., Kurki-Suonio, T., Suttrop, W., Stäbler, A., and the ASDEX Upgrade team, Plasma Physics and Controlled Fusion **50** (2008) 035014.
- [74] de Vries, P., Salmi, A., Parail, V., et al., Nuclear Fusion **48** (2008) 035007.
- [75] Johnson, T., Salmi, A., Steinbrecher, G., et al., Library for rf interactions in orbit following codes, in *Radio frequency power in plasmas: Proceedings of the 19th topical conference*, volume 1406, pp. 373–376, AIP Publishing, 2011.
- [76] Asunta, O., Govenius, J., Budny, R., et al., accepted for publication in Computer Physics Communications (2014).
- [77] Bosch, H.-S. and Hale, G., Nuclear Fusion **32** (1992) 611.
- [78] Brysk, H., Plasma Physics **15** (1973) 611.
- [79] Snicker, A., Kurki-Suonio, T., and Sipilä, S. K., Plasma Science, IEEE Transactions on **38** (2010) 2177 .

- [80] Boozer, A. H. and Kuo-Petravic, G., *Physics of Fluids* **24** (1981) 851.
- [81] Hirvijoki, E., Brizard, A., Snicker, A., and Kurki-Suonio, T., *Physics of Plasmas* **20** (2013) 092505.
- [82] Badouel, D., *An Efficient Ray-Polygon Intersection*, pp. 390–393., Graphics Gems, Academic Press, 1990.
- [83] Asunta, O., Äkäslompolo, S., Kurki-Suonio, T., et al., *Nuclear Fusion* **52** (2012) 094014.
- [84] Snicker, A., Sipilä, S., and Kurki-Suonio, T., *Nuclear Fusion* **52** (2012) 094011.
- [85] Rubinstein, R. Y. and Kroese, D. P., *Simulation and the Monte Carlo method*, volume 707, John Wiley & Sons, 2011.
- [86] Mazul, I., Alekseev, A., Belyakov, V., et al., *Fusion Engineering and Design* **87** (2012) 437 , Tenth International Symposium on Fusion Nuclear Technology (ISFNT-10).
- [87] Challis, C., Cordey, J., Hammén, H., et al., *Nuclear Fusion* **29** (1989) 563.
- [88] Siren, P., Current density modelling in jet and jt-60u identity plasma experiments, Master’s thesis, Aalto University, School of Electrical Engineering, 2013.
- [89] Salmi, A., Johnson, T., Parail, V., et al., *Contributions to Plasma Physics* **48** (2008) 77.
- [90] Keilhacker, M., Gibson, A., Gormezano, C., and Rebut, P., *Nuclear Fusion* **41** (2001) 1925.
- [91] Matthews, G., *Journal of Nuclear Materials* **438, Supplement** (2013) S2 , Proceedings of the 20th International Conference on Plasma-Surface Interactions in Controlled Fusion Devices.
- [92] Luxon, J., *Nuclear Fusion* **42** (2002) 614.
- [93] Neubauer, O., Czymek, G., Giesen, B., Hüttemann, P., and Sauer, M., *Fusion Science and Technology* **47** (2005) 77.
- [94] Korsholm, S. B., Bindslev, H., Meo, F., et al., *Review of scientific instruments* **77** (2006) 10E514.
- [95] *Nuclear Fusion* **47** (2007).
- [96] Giacomelli, L., Conroy, S., Gorini, G., et al., *Review of Scientific Instruments* **85** (2014) .
- [97] Tardocchi, M., Nocente, M., and Gorini, G., *Plasma Physics and Controlled Fusion* **55** (2013) 074014.
- [98] Kiptily, V. G., Cecil, F. E., and Medley, S. S., *Plasma Physics and Controlled Fusion* **48** (2006) R59.
- [99] Medley, S. S., Donné, A. J. H., Kaita, R., et al., *Review of Scientific Instruments* **79** (2008) .

- [100] ADAS, Atomic data and analysis software, <http://www.adas.ac.uk/>.
- [101] Kurki-Suonio, T., Hynönen, V., Suttrop, W., et al., Edge fast ion distribution, in Marco, F. D. and Vlad, G., editors, *33rd European Physical Society Conference on Plasma Physics Roma, June 19 - 23, 2006*, volume 30I of *europhysics conference abstracts*, 2006.
- [102] Jämsä, S., Kurki-Suonio, T., Suttrop, W., et al., Benchmarking the fully 3d ascot-code against experimental npa data from ASDEX Upgrade, in *Proc. 36th EPS Conference on Plasma Physics*, p. P1.148, Sofia, Bulgaria, 2009.
- [103] Jämsä, S. J., Hirvijoki, E., Kurki-Suonio, T., and Pütterich, T., Implementing beam-beam CX-reactions in the ASCOT-code and prediction of active NPA measurement, in *Proc. 37th EPS Conference on Plasma Physics*, Europhysics Conference Abstracts, p. P1.148, Dublin, Ireland, 2010.
- [104] Heidbrink, W., Review of Scientific Instruments **81** (2010) 10D727.
- [105] Geiger, B., Garcia-Munoz, M., Heidbrink, W., et al., Plasma Physics and Controlled Fusion **53** (2011) 065010.
- [106] Jones, O. M., Michael, C. A., McClements, K. G., et al., Plasma Physics and Controlled Fusion **55** (2013) 085009.
- [107] Heidbrink, W., Liu, D., Luo, Y., Ruskov, E., and Geiger, B., Comm. Comp. Physics **8** (2010).
- [108] Salewski, M., Geiger, B., Jacobsen, A., et al., Nuclear Fusion **54** (2014) 023005.
- [109] Bindslev, H., Nielsen, S., Porte, L., et al., Physical review letters **97** (2006) 205005.
- [110] Salewski, M., Asunta, O., Eriksson, L.-G., et al., Plasma Physics and Controlled Fusion **51** (2009) 035006.
- [111] Salewski, M., Geiger, B., Nielsen, S., et al., Nuclear Fusion **53** (2013) 063019.
- [112] Darrow, D. S., Bäuml, S., Cecil, F. E., et al., Review of Scientific Instruments **75** (2004) 3566.
- [113] Fisher, R., Pace, D., García-Muñoz, M., et al., Review of Scientific Instruments **81** (2010) 10D307.
- [114] Salmi, A. T., Tala, T., Corrigan, G., et al., Plasma Physics and Controlled Fusion **53** (2011) 085005.
- [115] Hinton, F. and Wong, S., Physics of Fluids (1958-1988) **28** (1985) 3082.
- [116] Wesson, J., Nuclear Fusion **37** (1997) 577.
- [117] Angioni, C., Mantica, P., Pütterich, T., et al., Nuclear Fusion **54** (2014) 083028.
- [118] Fischer, O., Cooper, W., Isaev, M., and Villard, L., Nuclear Fusion **42** (2002) 817.

- [119] Zehrfeld, H., Resistive equilibrium states of axisymmetric plasmas with compressible viscous fluid flow, in *26th EPS Conference on Controlled Fusion*, 1999.
- [120] Kramer, G. J., Budny, R. V., Bortolon, A., et al., *Plasma Physics and Controlled Fusion* **55** (2013) 025013.
- [121] Spong, D., Hirshman, S., and Whitson, J., *Plasma Physics Reports* **23** (1997) 483.
- [122] Shimada, M., Campbell, D., Mukhovatov, V., et al., *Nuclear Fusion* **47** (2007) S1.
- [123] Sips, A. C. C., *Plasma Physics and Controlled Fusion* **47** (2005) A19.
- [124] Connor, J., Fukuda, T., Garbet, X., et al., *Nuclear Fusion* **44** (2004) R1.
- [125] Badouel, D., *Graphics gems*, chapter An efficient ray-polygon intersection, pp. 390–393, Academic Press Professional, Inc., San Diego, CA, USA, 1990.
- [126] Koskela, T., Asunta, O., Kurki-Suonio, T., et al., Ascot simulations of fast ion wall loads on the iter first wall in the presence and absence of port limiters, in *Proc. 36th EPS Conference on Plasma Physics*, p. P4.160, Sofia, Bulgaria, 2009.
- [127] Lackner, K., Private communication, 2009.
- [128] Shinohara, K., Oikawa, T., Urano, H., et al., *Fusion Engineering and Design* **84** (2009) 24 .
- [129] Shinohara, K., Kurki-Suonio, T., Spong, D., et al., *Nuclear Fusion* **51** (2011) 063028.
- [130] Lamzin, E. A., Amoskov, V. M., Gapionok, E. I., et al., *Applied Superconductivity*, IEEE Transactions on **22** (2012) 4901004.
- [131] Shinohara, K., Tani, K., Oikawa, T., et al., *Nuclear Fusion* **52** (2012) 094008.
- [132] Tani, K., Shinohara, K., Oikawa, T., et al., *Nuclear Fusion* **52** (2012) 013012.
- [133] Orain, F., Bécoulet, M., Dif-Pradalier, G., et al., *Physics of Plasmas* (1994-present) **20** (2013) .
- [134] Baranov, Y. F., Jenkins, I., Alper, B., et al., *Plasma Physics and Controlled Fusion* **51** (2009) 044004.

Nuclear fusion holds the promise of clean, safe and abundant energy for the future generations. It would be foolish not to explore its full potential, especially now when we desperately need new energy sources. In order to achieve controlled fusion, a plasma suspended in vacuum by a magnetic field must be heated to a temperature higher than the core of the sun. Today this is routinely achieved in experimental facilities worldwide.

In order for a fusion reactor to *produce* energy, it must be able to maintain its temperature with little external heating. The key to achieving a burning fusion plasma is understanding the behavior of the fast ions that carry a fraction of the energy released in the fusion reactions. This thesis studies the physics of fast ions whose orbits are perturbed by the breaking of axisymmetry in a tokamak reactor. It is vital for the operation of ITER, the next generation fusion experiment that aims at demonstrating the feasibility of fusion power in the 2020s.



ISBN 978-952-60-6003-3 (printed)
ISBN 978-952-60-6004-0 (pdf)
ISSN-L 1799-4934
ISSN 1799-4934 (printed)
ISSN 1799-4942 (pdf)

Aalto University
School of Science
Applied Physics
www.aalto.fi

BUSINESS +
ECONOMY

ART +
DESIGN +
ARCHITECTURE

SCIENCE +
TECHNOLOGY

CROSSOVER

DOCTORAL
DISSERTATIONS